

Chapter 2

New Anion Exchangeable Layered Lanthanide Hydroxides: Their Synthesis, Characterisation and Properties

2.0 Introduction

A review of the literature surrounding layered hydroxides reveals their remarkable compositional flexibility. Notably however the range of cationic radii which can be incorporated into LDHs remains relatively limited, primarily to Mg^{2+} , Al^{3+} and the first row transition metals (section 1.3.1). It can be envisaged that the incorporation of rare-earth cations into layered hydroxide materials would offer the potential to combine the optical, magnetic and catalytic properties of the lanthanides with the flexibility of intercalation hosts.

There are reports of lanthanide-containing complexes being intercalated into the interlayer gallery of layered double hydroxides. Chang *et al.* have intercalated $\text{Ln}(\text{dipic})_3^{3+}$ ($\text{Ln} = \text{Eu}, \text{Ce}$; $\text{dipic} = \text{C}_7\text{H}_3\text{NO}_4$) into various LDHs and note that the luminescence properties of the Eu complex could allow its use as a structural probe for other layered hydroxide structures.¹ Gago *et al.* have used ZnAl LDH pillared by 2,2'-bipyridine-5,5'-dicarboxylate anions as a porous matrix into which they have incorporated LnCl_3 ($\text{Ln} = \text{Gd}, \text{Eu}$).²

The larger lanthanides are known to form layered hydroxynitrates with the general formula $\text{Ln}(\text{OH})_2\text{NO}_3 \cdot x\text{H}_2\text{O}$ ($\text{Ln} = \text{La}, \text{Pr}, \text{Nd}, \text{Sm}$ and Gd ; $x = 0, 1$).³⁻⁶ Anion exchange has been demonstrated for reaction of $\text{La}(\text{OH})_2\text{NO}_3 \cdot \text{H}_2\text{O}$ with acetate, benzoate and terephthalate salts.⁷ The structure consists of lanthanum hydroxide layers in which La^{3+} is 9-coordinate with the interlayer nitrate anions coordinated directly to the metal in an approximately perpendicular orientation (Figure 1). This coordination of the metal cation with the interlayer species meant that room temperature anion exchange reactions proved unsuccessful, and in order to facilitate anion exchange, reactions needed to be carried out at 65 °C for 7 days.

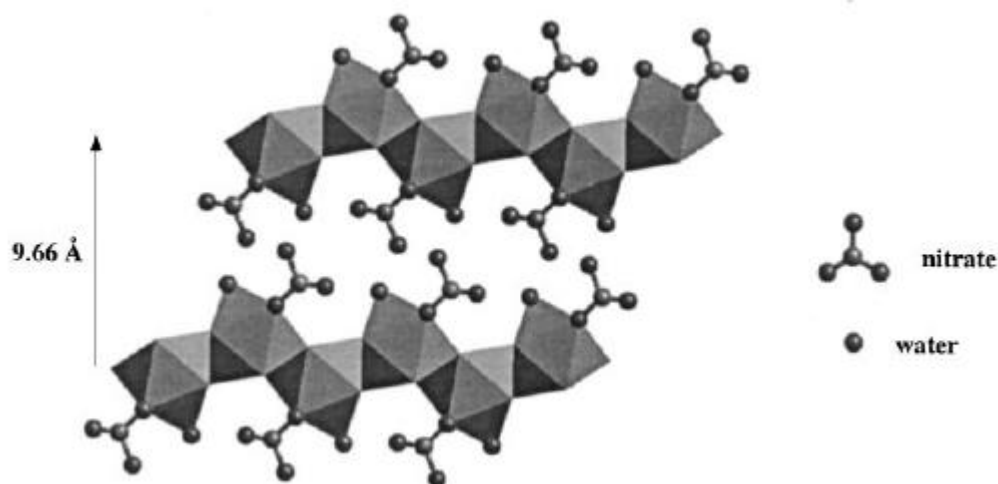


Figure 1 Schematic representation of the structure of $\text{La}(\text{OH})_2\text{NO}_3\cdot\text{H}_2\text{O}$.⁷

Materials with the composition $\text{Ln}_2(\text{OH})_5\text{NO}_3\cdot 2\text{H}_2\text{O}$ ($\text{Ln} = \text{Y}, \text{Yb}$) have also been described.⁸⁻¹⁰ In a comprehensive study of the preparation of lanthanide hydroxide nitrates Haschke reports the hydrothermal synthesis of orthorhombic $\text{Y}_2(\text{OH})_5\text{NO}_3\cdot 2\text{H}_2\text{O}$ and $\text{Yb}_2(\text{OH})_5\text{NO}_3\cdot 2\text{H}_2\text{O}$ with unit cell parameters $a \sim 6.0 \text{ \AA}$, $b \sim 3.8 \text{ \AA}$ and $c \sim 8.5 \text{ \AA}$.⁸ The study also revealed several related, non-stoichiometric phases with the compositions including $\text{Ln}_2(\text{OH})_{5.14}(\text{NO}_3)_{0.86}$ ($\text{Ln} = \text{La}, \text{Pr}$ and Nd), $\text{Ln}_2(\text{OH})_{5.39}(\text{NO}_3)_{0.61}$ ($\text{Ln} = \text{Sm} - \text{Dy}, \text{Yb}$) as well as the stoichiometric materials, $\text{Ln}(\text{OH})_2\text{NO}_3$ ($\text{Ln} = \text{La}, \text{Pr}, \text{Nd}, \text{Sm} - \text{Dy}$).

The hydrothermal synthesis of $[\text{Ln}_4(\text{OH})_{10}(\text{H}_2\text{O})_4]\text{A}$ ($\text{Ln} = \text{Y}, \text{Dy}, \text{Ho}, \text{Yb}$; $\text{A} = 2,6$ -naphthalenedisulfonate, 2,6-anthraquinonedisulfonate) phases were reported by Gándara *et al.*¹¹ Single crystal diffraction studies revealed an orthorhombic structure for the Y-2,6-naphthalenedisulfonate and Yb-2,6-anthraquinonedisulfonate materials. The positively charged $[\text{Ln}_4(\text{OH})_{10}(\text{H}_2\text{O})_4]^{2+}$ layers consist of 8- and 9-coordinate lanthanide cations. 8-coordinated Ln^{3+} lanthanide cations are coordinated to μ_3 -hydroxy groups and one water atom giving rise to two different polyhedra; a dodecahedron and a monocapped square antiprism. The organic anions are located between the layers and are ordered through hydrogen bonding interactions with the layers. These materials are shown to act efficiently as heterogeneous catalysts in hydrodesulfurization, sulfide oxidation and redox reactions.

2.1 Scope of chapter

This chapter describes the hydrothermal synthesis and anion exchange capacity of some new anion exchange host lattices containing the smaller lanthanide cations, with the composition $\text{Ln}_2(\text{OH})_5\text{NO}_3 \cdot 1.5\text{H}_2\text{O}$ ($\text{Ln} = \text{Y}, \text{Gd} - \text{Lu}$). An investigation in to their selective anion exchange, selectivity and optical properties has been carried out. These new lanthanide containing hydroxycyanion materials have also been expanded to include $\text{Ln}_2(\text{OH})_5\text{X} \cdot 1.5\text{H}_2\text{O}$ ($\text{X} = \text{Cl}, \text{Br}; \text{Ln} = \text{Y}, \text{Dy}, \text{Er}, \text{Yb}$).

2.2 $\text{Ln}_2(\text{OH})_5\text{NO}_3 \cdot 1.5\text{H}_2\text{O}$ ($\text{Ln} = \text{Y}, \text{Gd} - \text{Lu}$) - A Novel Family of Anion Exchange Intercalation Hosts

2.2.1 Synthesis and Characterisation

A novel family of hydroxynitrates, containing the smaller lanthanide cations, have been prepared. The $\text{Ln}_2(\text{OH})_5\text{NO}_3 \cdot 1.5\text{H}_2\text{O}$ ($\text{Ln} = \text{Y}, \text{Gd} - \text{Lu}$) phases are synthesised from an aqueous solution of $\text{Ln}(\text{NO}_3)_3 \cdot x\text{H}_2\text{O}$, NaOH and NaNO_3 treated hydrothermally at $150\text{ }^\circ\text{C}$ ($125\text{ }^\circ\text{C}$ for Y) for 48 hours.

The phase purity of these materials is confirmed by powder XRD for the samples with $\text{Ln} = \text{Y}, \text{Tb} - \text{Tm}$, however those with Gd, Yb and Lu were always found to contain impurities. The Yb and Lu materials were not isolated phase pure, for both materials a second phase displaying a slightly larger interlayer separation of approximately 9.40 \AA is apparent in the powder XRD data, as shown in Figure 2. Analysis of the bulk material via TGA and elemental analysis indicates that these two phases have similar compositions, and are therefore different from the related phases reported by Haschke.⁸ The Yb host lattice will be the subject of further discussion in Chapter 3 of this thesis.

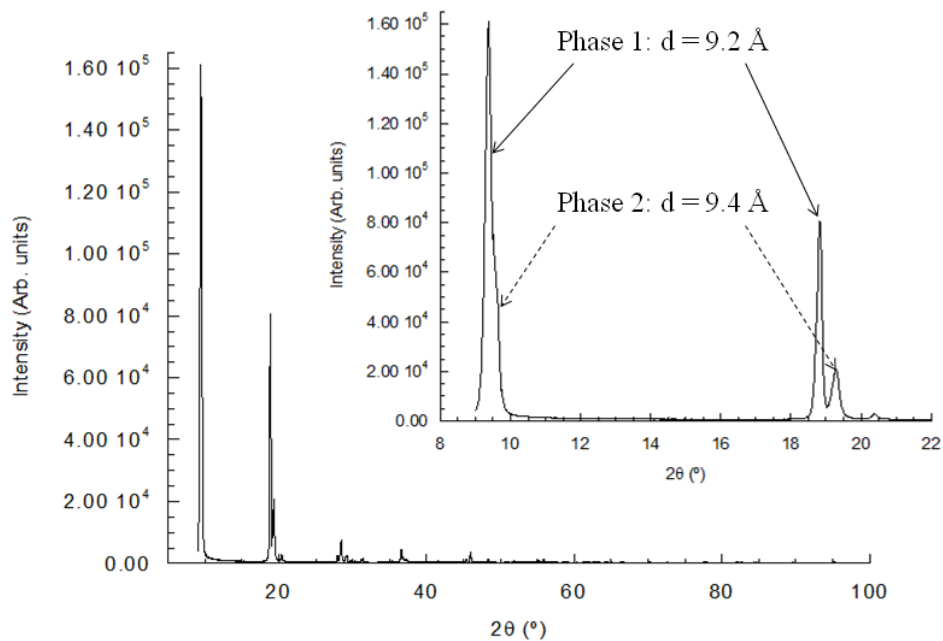


Figure 2 Powder X-ray diffraction pattern of $\text{Yb}_2(\text{OH})_5\text{NO}_3 \cdot x\text{H}_2\text{O}$. INSET: Expanded region showing the presence of a second phase.

Powder X-ray diffraction data, shown in Figure 3, indicate that $\text{Gd}_2(\text{OH})_5\text{NO}_3 \cdot 1.5\text{H}_2\text{O}$ is less crystalline than the other materials, suggesting that Gd marks the limiting cation size for this phase. In addition a small amount of impurity phase; possibly GdONO_3 is always present in the sample.^{8, 12}

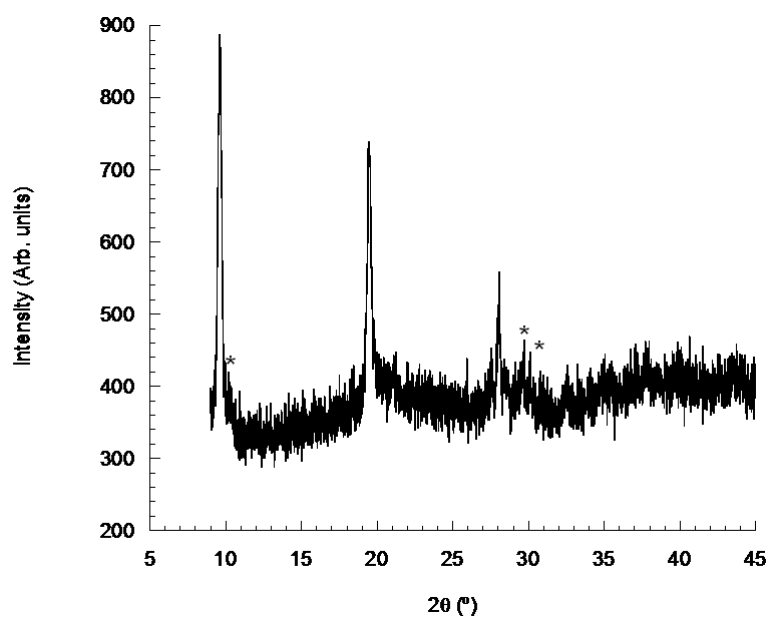


Figure 3 Powder X-ray diffraction pattern of as synthesised, impure $\text{Gd}_2(\text{OH})_5\text{NO}_3 \cdot 1.5\text{H}_2\text{O}$.

* Indicates reflections attributed to the presence of GdONO_3 .

Reactions with the larger lanthanides (La – Eu) under the same conditions yield a mixture of the Ln_2O_3 , $\text{Ln}(\text{OH})_2\text{NO}_3 \cdot 1.5\text{H}_2\text{O}$ and $\text{Ln}(\text{OH})_3$ as products with the precise combination dependant on lanthanide used.

The composition of the $\text{Ln}_2(\text{OH})_5\text{NO}_3 \cdot 1.5\text{H}_2\text{O}$ ($\text{Ln} = \text{Y}, \text{Tb} - \text{Lu}$) phases has been determined by elemental analysis and TGA, the characterising data is summarized in Table 1.

Table 1 Characterising data for the new layered lanthanide hydroxides, $\text{Ln}_2(\text{OH})_5\text{NO}_3 \cdot 1.5\text{H}_2\text{O}$ ($\text{Ln} = \text{Y}, \text{Tb} - \text{Tm}$).

Ln	Composition	Interlayer Separation (Å)	Elemental Analysis	
			Observed (%)	Calculated (%)
Y [†]	$\text{Y}_2(\text{OH})_5\text{NO}_3 \cdot 1.5\text{H}_2\text{O}$	9.18	Y (49.89) N (3.91) H (2.25)	Y (50.53) N (3.98) H (2.29)
Tb	$\text{Tb}_2(\text{OH})_5\text{NO}_3 \cdot 1.5\text{H}_2\text{O}$	9.06	Tb (62.66) N (2.55) H (1.53)	Tb (64.61) N (2.85) H (1.64)
Dy	$\text{Dy}_2(\text{OH})_5\text{NO}_3 \cdot 1.5\text{H}_2\text{O}$	9.06	Dy (63.71) N (3.00) H (1.55)	Dy (65.12) N (2.81) H (1.62)
Ho	$\text{Ho}_2(\text{OH})_5\text{NO}_3 \cdot 1.5\text{H}_2\text{O}$	9.10	Ho (59.89) N (2.34) H (1.45)	Ho (65.46) N (2.78) H (1.60)
Er	$\text{Er}_2(\text{OH})_5\text{NO}_3 \cdot 1.5\text{H}_2\text{O}$	9.28	Er (65.20) N (2.82) H (1.54)	Er (65.77) N (2.75) H (1.59)
Tm	$\text{Tm}_2(\text{OH})_5\text{NO}_3 \cdot 1.5\text{H}_2\text{O}$	9.14	Tm (60.55) N (2.46) H (1.39)	Tm (65.99) N (2.73) H (1.58)

[†] $\text{Y}_2(\text{OH})_5\text{NO}_3 \cdot 1.5\text{H}_2\text{O}$ synthesised by Miss L. K. Jackson.

These materials are isostructural and have comparable analytical data and therefore will be exemplified here by the Er phase. Characterising data on the other compounds and full details of their anion exchange reactions are provided in the Appendices.

The TGA data for $\text{Er}_2(\text{OH})_5\text{NO}_3 \cdot 1.5\text{H}_2\text{O}$ is shown in Figure 4 and displays three distinct mass losses comparable to those seen for other layered hydroxides. The first mass loss of 4.35 % (calculated value for $x = 1.5$ is 5.21 %) below 150 °C corresponds to the loss of co-intercalated water. The second mass loss of 7.24 % (7.19 %) by 350 °C corresponds to partial decomposition of the layers leaving a material of nominal composition ' $\text{Er}_2\text{O}_2(\text{OH})\text{NO}_3$ '.¹⁰ By 650 °C final decomposition to Er_2O_3 is complete with a mass loss of 11.68 % (12.39 %). No further mass loss is observed above 650 °C.

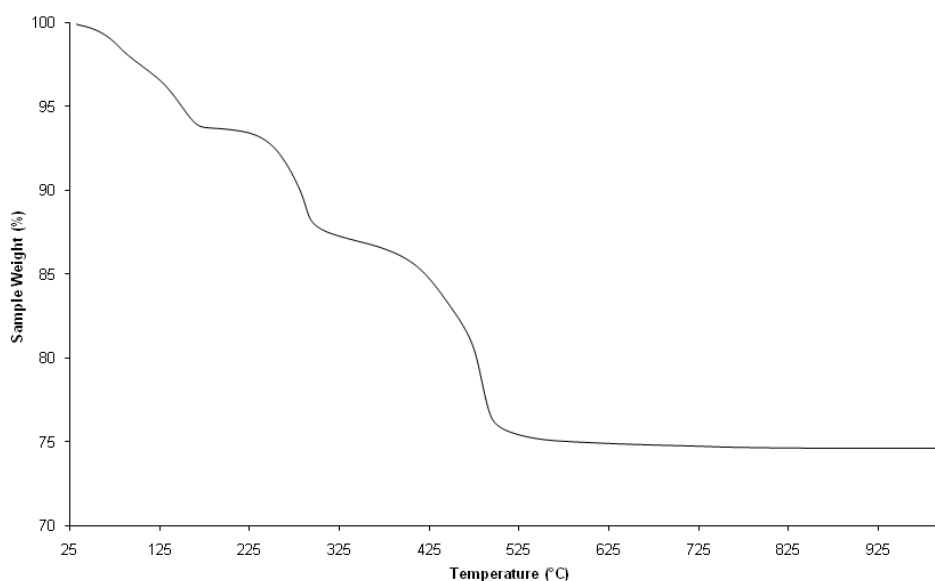


Figure 4 TGA trace for $\text{Er}_2(\text{OH})_5\text{NO}_3 \cdot 1.5\text{H}_2\text{O}$ showing mass losses of 4.35 % below 150 °C and further mass losses of 7.24 % by 350 °C and 11.68 % by 650 °C.

SEM reveals that these new phases comprise microcrystalline powders and display an approximately hexagonal plate-like morphology (Figure 5). A typical powder XRD pattern, for $\text{Er}_2(\text{OH})_5\text{NO}_3 \cdot 1.5\text{H}_2\text{O}$, is shown in Figure 6. The series of strong (00 l) reflections is characteristic of a layered phase and corresponds to an interlayer

separation of 9.28 Å. Unlike many other layered hydroxides, there are also a significant number of relatively weak non-(00 l) reflections indicating that the layers are ordered.

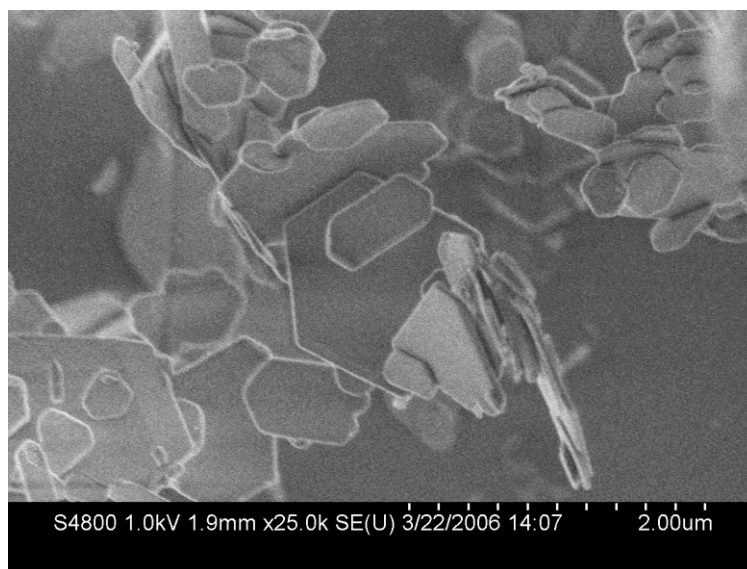


Figure 5 SEM image of Y₂(OH)₅NO₃·1.5H₂O (image taken by Dr. M. Allix).

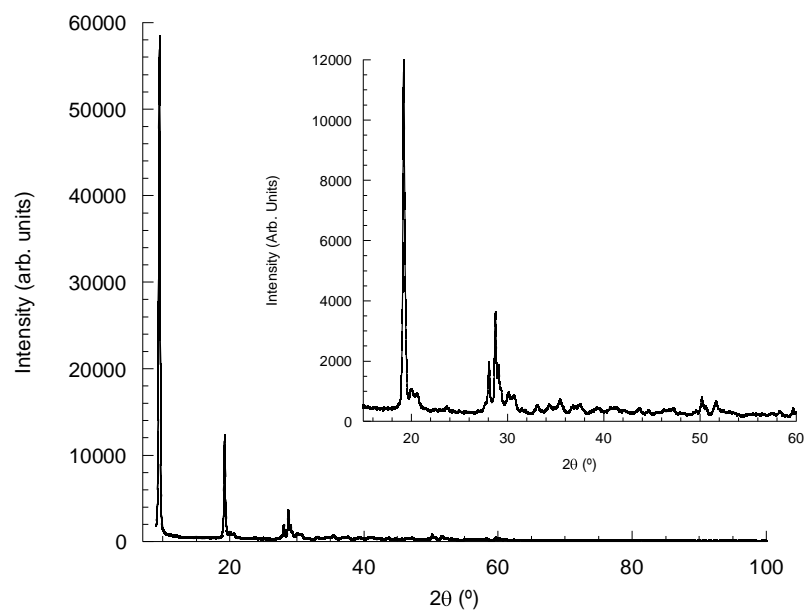


Figure 6 Powder X-ray diffraction pattern of Er₂(OH)₅NO₃·1.5H₂O. INSET Enlarged diffraction pattern covering the 2θ range 15 - 60 °.

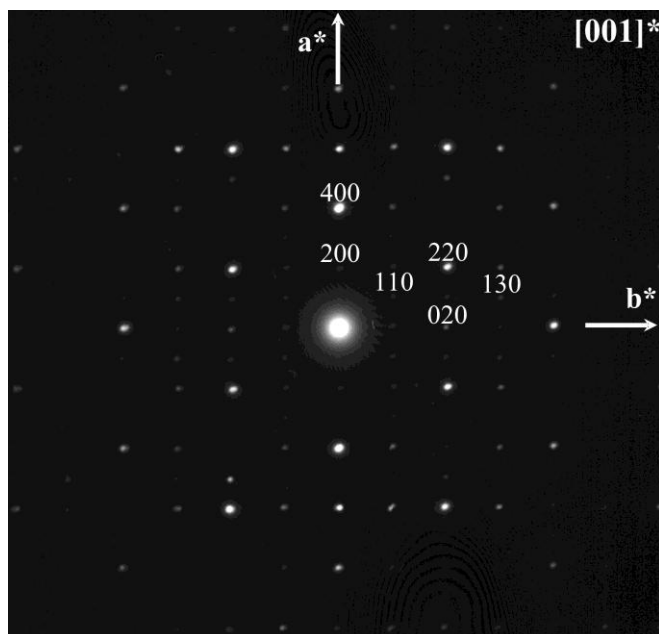


Figure 7 Selected area electron diffraction pattern of $\text{Er}_2(\text{OH})_5\text{NO}_3 \cdot 1.5\text{H}_2\text{O}$ (Dr. M. Allix).

This order within the ab plane is confirmed by electron diffraction. The SAED pattern shown in Figure 7 indicates lattice parameters of $a \sim 7.1 \text{ \AA}$ and $b \sim 12.7 \text{ \AA}$. No systematic absences were found for this plane, however it was not possible to observe diffraction from along the c -axis. Tilting of the samples produced little change in the diffraction patterns indicative of extensive layer stacking faults within the crystal along the c -axis. This has been previously observed in other layered systems.¹³

The disorder inherent in these materials has prevented both a full structure determination from powder XRD data and the synthesis of diffraction quality single crystals of any of these phases (despite extensive screening of the reaction conditions through variation of reagent concentrations, reaction temperature and time and control of cooling rate). The a and b parameters observed by electron diffraction combined with the interlayer separation confirm that these materials are structurally different from the orthorhombic ones reported by Haschke ($a = 6.064(4) \text{ \AA}$, $b = 3.800(1) \text{ \AA}$ and $c = 8.533(3) \text{ \AA}$ for $\text{Y}_2(\text{OH})_5\text{NO}_3 \cdot 2\text{H}_2\text{O}$). This indicates the possibility of polymorphism in this system or perhaps suggests that only small changes in hydration can have a significant effect on structure.

It is likely that the structure of these $\text{Ln}_2(\text{OH})_5\text{NO}_3 \cdot 1.5\text{H}_2\text{O}$ materials is related to the $[\text{Ln}_4(\text{OH})_{10}(\text{H}_2\text{O})_4]\text{A}$ ($\text{Ln} = \text{Y, Dy, Ho, Yb}$; $\text{A} = 2,6\text{-naphthalenedisulfonate (NDS), 2,6-anthraquinonedisulfonate (AQDS)}$) phases reported by Gándara *et al.*¹¹ The lattice parameters for the orthorhombic structure for the Y-2,6-naphthalenedisulfonate ($a = 12.639(1) \text{ \AA}$, $b = 30.525(2) \text{ \AA}$, $c = 7.1348(6) \text{ \AA}$) and Yb-2,6-anthraquinonedisulfonate are comparable to those seen for the nitrate materials described herein suggesting a similar layer structure. In the YNDS and YbAQDS materials, the $[\text{Ln}_4(\text{OH})_{10}(\text{H}_2\text{O})_4]^{2+}$ layers comprise 8- and 9-coordinated lanthanide cations, with bridging μ_3 -hydroxy groups and one water molecule giving rise to a dodecahedron and a monocapped square antiprism (Chapter 1, Figure 10). The interlayer NDS and AQDS anions are not bound to Ln^{3+} and are ordered through hydrogen bonding interactions with the layers. It was not possible to index the powder diffraction data of the $\text{Ln}_2(\text{OH})_5\text{NO}_3 \cdot 1.5\text{H}_2\text{O}$ materials to an orthorhombic cell despite these similarities in lattice parameters. Instead it was indexed to a monoclinic cell with $a = 7.0808(4) \text{ \AA}$, $b = 12.7005(5) \text{ \AA}$, $c = 18.6348(4) \text{ \AA}$ and $\beta = 92.509(5)^\circ$. The Le Bail fit for this cell is shown in Figure 8.

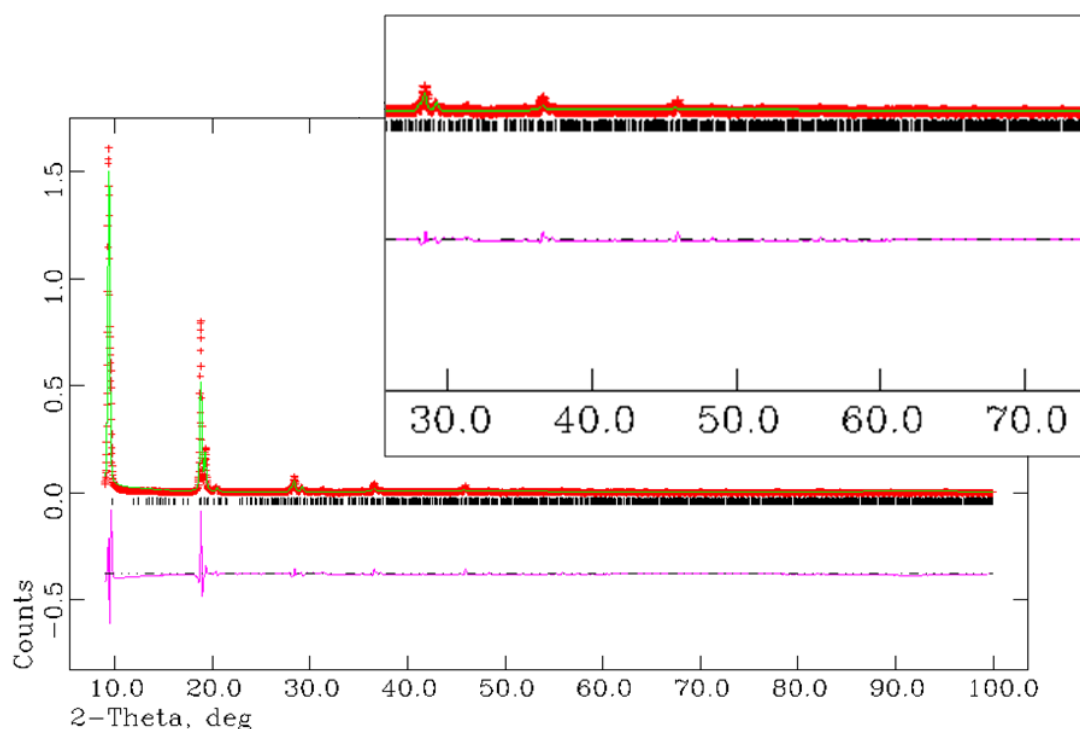


Figure 8 Le Bail refinement fit for $\text{Er}_2(\text{OH})_5\text{NO}_3 \cdot 1.5\text{H}_2\text{O}$. INSET expanded region covering the 2θ range $30 - 70^\circ$.

The FTIR spectrum of $\text{Er}_2(\text{OH})_5\text{NO}_3 \cdot 1.5\text{H}_2\text{O}$ is shown in Figure 9 and is representative of all the host materials. The data is in agreement with the presence of an uncoordinated nitrate anion located between the $[\text{Er}_2(\text{OH})_5]^+$ layers (broad band at approximately 1370 cm^{-1}) and is comparable to observations made on other layered hydroxides containing interlayer nitrate groups.^{7, 14} Other key features in the spectrum are a broad absorption band at approximately 3500 cm^{-1} corresponding to a combination of the stretching vibrations of the layer hydroxyl groups and the interlayer water molecules and the bending vibration of water at 1630 cm^{-1} .

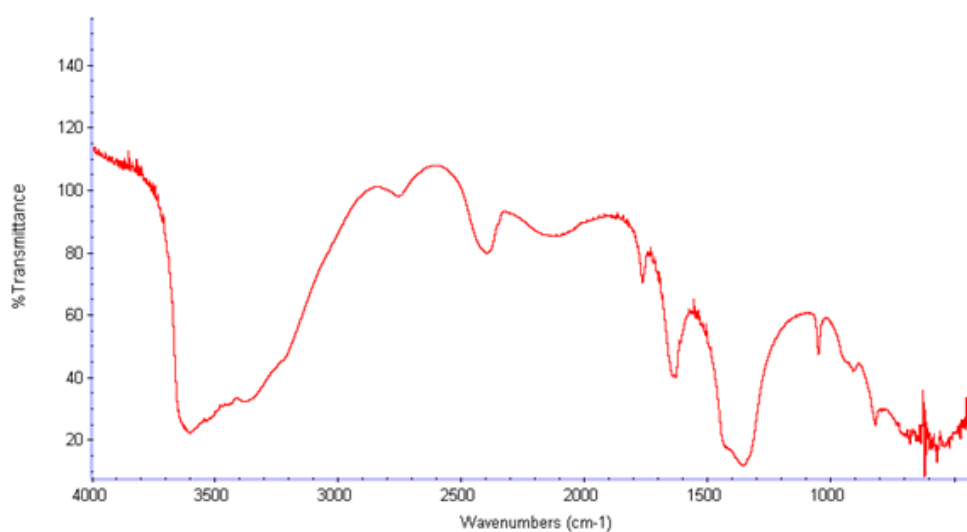


Figure 9 FTIR spectrum of $\text{Er}_2(\text{OH})_5\text{NO}_3 \cdot 1.5\text{H}_2\text{O}$.

The characterising data discussed above for the $\text{Ln}_2(\text{OH})_5\text{NO}_3 \cdot 1.5\text{H}_2\text{O}$ ($\text{Ln} = \text{Y}, \text{Gd} - \text{Lu}$) phases are consistent with the formation of layered hydroxynitrates which incorporate the smaller lanthanide cations within the layers and have non-coordinated charge balancing nitrate anions between them.

2.2.2 Anion Exchange Reactions

One characteristic property of the LDHs and other layered hydroxides is the ability to undergo anion exchange reactions with a variety of anions. For the $\text{Ln}_2(\text{OH})_5\text{NO}_3 \cdot 1.5\text{H}_2\text{O}$ ($\text{Ln} = \text{Y}, \text{Tb} - \text{Tm}$) phases anion exchange has been

demonstrated with a range of organic carboxylates and sulfonates for all of the host lattices. For the most part, reactions proceed successfully at room temperature in a few minutes. Complete anion exchange was confirmed both by the absence of reflections characteristic of the host lattice in the powder XRD patterns and of nitrogen in the elemental analysis. Reactions with smaller anions, such as oxalate and malonate for some host materials proved to be incomplete and therefore formulae containing both nitrate and the organic anion are reported. Successful anion exchange reactions, yielding $\text{Ln}_2(\text{OH})_5\text{A}_{0.5}\cdot x\text{H}_2\text{O}$ ($x \approx 1.5$) for dianions, have been observed with dicarboxylates, including succinate, suberate, fumarate, maleate, phthalate and terephthalate, and sulfonates, for example decylsulfonate and 2,6-naphthalenedisulfonate. Typical powder X-ray diffraction patterns of the anion exchange derivatives of $\text{Er}_2(\text{OH})_5\text{NO}_3\cdot 1.5\text{H}_2\text{O}$ are shown in Figure 10 and the characterising data for the materials in summarized in Table 2.

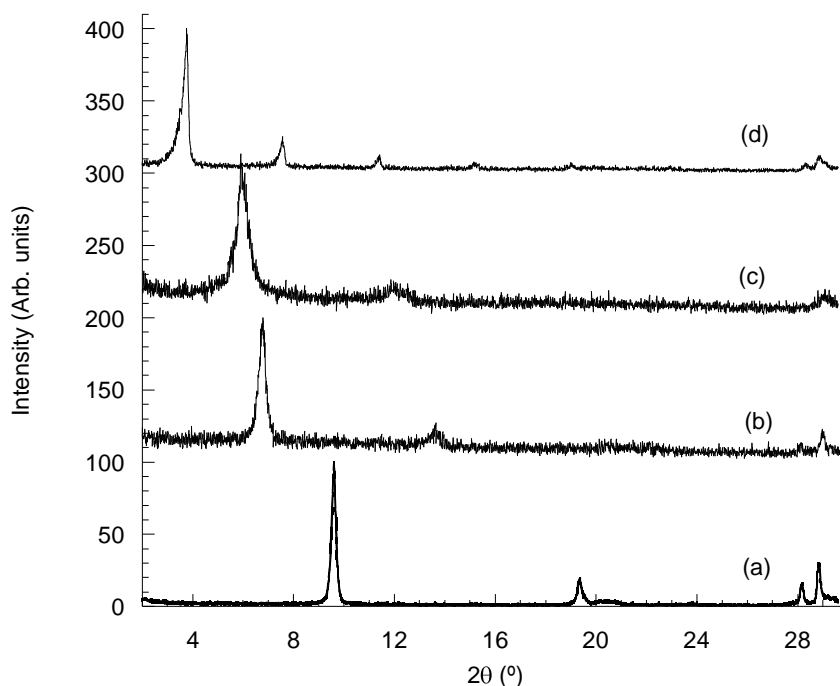


Figure 10 Powder XRD diffraction patterns of:

- (a) $\text{Er}_2(\text{OH})_5\text{NO}_3\cdot 1.5\text{H}_2\text{O}$ and the anion exchange intercalation compounds
- (b) $\text{Er}_2(\text{OH})_5(p\text{-C}_6\text{H}_4(\text{CO}_2)_2)_{0.5}\cdot 1.5\text{H}_2\text{O}$,
- (c) $\text{Er}_2(\text{OH})_5(\text{C}_8\text{H}_{12}\text{O}_4)_{0.5}\cdot 1.5\text{H}_2\text{O}$ and
- (d) $\text{Er}_2(\text{OH})_5(\text{C}_{10}\text{H}_{21}\text{OSO}_3)_{1.5}\text{H}_2\text{O}$.

Table 2 Characterising data for the organic anion exchange derivatives of $\text{Er}_2(\text{OH})_5\text{NO}_3 \cdot 1.5\text{H}_2\text{O}$.

Anion	Composition	Interlayer Separation (Å)	Elemental Analysis	
			Observed (%)	Calculated (%)
Maleate	$\text{Er}_2(\text{OH})_5(\text{cis-C}_4\text{H}_2\text{O}_4)_{0.5} \cdot 1.5\text{H}_2\text{O}$	9.4	Er (65.25)	Er (66.42)
			C (4.93)	C (4.77)
			H (1.76)	H (1.80)
Fumarate	$\text{Er}_2(\text{OH})_5(\text{trans-C}_4\text{H}_2\text{O}_4)_{0.5} \cdot 1.5\text{H}_2\text{O}$	9.6	Er (65.90)	Er (66.42)
			C (4.66)	C (4.77)
			H (1.78)	H (1.80)
Phthalate	$\text{Er}_2(\text{OH})_5(o\text{-C}_8\text{H}_4\text{O}_4)_{0.5} \cdot \text{H}_2\text{O}$	14.0	Er (58.87)	Er (63.16)
			C (8.99)	C (9.24)
			H (2.08)	H (1.75)
Terephthalate	$\text{Er}_2(\text{OH})_5(p\text{-C}_8\text{H}_4\text{O}_4)_{0.5} \cdot \text{H}_2\text{O}$	13.1	Er (58.87)	Er (63.16)
			C (9.42)	C (9.24)
			H (2.06)	H (1.75)
Oxalate	$\text{Er}_2(\text{OH})_5(\text{C}_2\text{O}_4)_{0.45}(\text{NO}_3)_{0.1} \cdot 1.5\text{H}_2\text{O}$	7.98	C (2.26)	C (2.19)
			H (1.41)	H (1.64)
			N (0.29)	N (0.28)
Malonate	$\text{Er}_2(\text{OH})_5(\text{C}_3\text{H}_2\text{O}_4)_{0.5} \cdot 1.5\text{H}_2\text{O}$	11.2	Er (66.91)	Er (67.23)
			C (3.64)	C (3.62)
			H (1.80)	H (1.82)
Succinate	$\text{Er}_2(\text{OH})_5(\text{C}_4\text{H}_4\text{O}_4)_{0.5} \cdot 1.5\text{H}_2\text{O}$	9.8	Er (66.07)	Er (66.29)
			C (4.68)	C (4.76)
			H (1.98)	H (1.99)
Glutarate	$\text{Er}_2(\text{OH})_5(\text{C}_5\text{H}_6\text{O}_4)_{0.5} \cdot 1.5\text{H}_2\text{O}$	10.4	Er (63.68)	Er (65.38)
			C (6.00)	C (5.87)
			H (2.21)	H (2.17)
Suberate	$\text{Er}_2(\text{OH})_5(\text{C}_8\text{H}_{12}\text{O}_4)_{0.5} \cdot \text{H}_2\text{O}$	14.8	Er (60.80)	Er (62.80)
			C (10.12)	C (9.17)
			H (2.70)	H (2.50)
Decylsulfonate	$\text{Er}_2(\text{OH})_5(\text{C}_{10}\text{H}_{21}\text{SO}_4) \cdot 1.5\text{H}_2\text{O}$	23.9	Er (50.37)	Er (48.91)
			C (17.52)	C (17.56)
			H (4.20)	H (4.27)
NDS	$\text{Er}_2(\text{OH})_5(\text{C}_{10}\text{H}_6(\text{SO}_3)_2)_{0.28}(\text{NO}_3)_{0.44} \cdot 3\text{H}_2\text{O}$	15.6	Er (57.19)	Er (57.57)
			C (4.69)	C (5.78)
			H (1.64)	H (2.19)
			N (0.73)	N (1.06)

AQDS	$\text{Er}_2(\text{OH})_5(\text{C}_{14}\text{H}_6\text{O}_2(\text{SO}_3)_2)_{0.22}(\text{NO}_3)_{0.54}\cdot 3\text{H}_2\text{O}$	18.2	Er (55.46)	Er (56.74)
			C (5.14)	C (6.27)
			H (1.63)	H (2.10)
			N (1.10)	N (1.35)

FTIR spectra of the anion exchange product $\text{Er}_2(\text{OH})_5(\text{C}_4\text{H}_4\text{O}_4)_{0.5}\cdot 1.5\text{H}_2\text{O}$ and succinic acid disodium salt are shown in Figure 11. The spectrum for sodium succinate displays characteristic bands in the regions 1550 cm^{-1} and 1400 cm^{-1} and further absorptions at $1220 - 1170\text{ cm}^{-1}$ and 920 cm^{-1} .¹⁵ The spectrum for the exchange product shows the presence of symmetric and asymmetric COO^- stretches from the succinate anions (approximately 1550 cm^{-1} and 1400 cm^{-1} respectively) providing further evidence of successful reaction. The broad absorption band at 3300 cm^{-1} is due to hydroxide and interlayer H_2O stretches.¹⁶ Comparison with the FTIR spectra of $\text{Er}_2(\text{OH})_5\text{NO}_3\cdot 1.5\text{H}_2\text{O}$ (Figure 9) further demonstrates anion exchange with the absence of the broad band at 1370 cm^{-1} (uncoordinated nitrate). A very small band at 1300 cm^{-1} may be attributed to the presence of a small amount of residual nitrate or carbonate in the interlayer region; however this is not detected by elemental analysis.

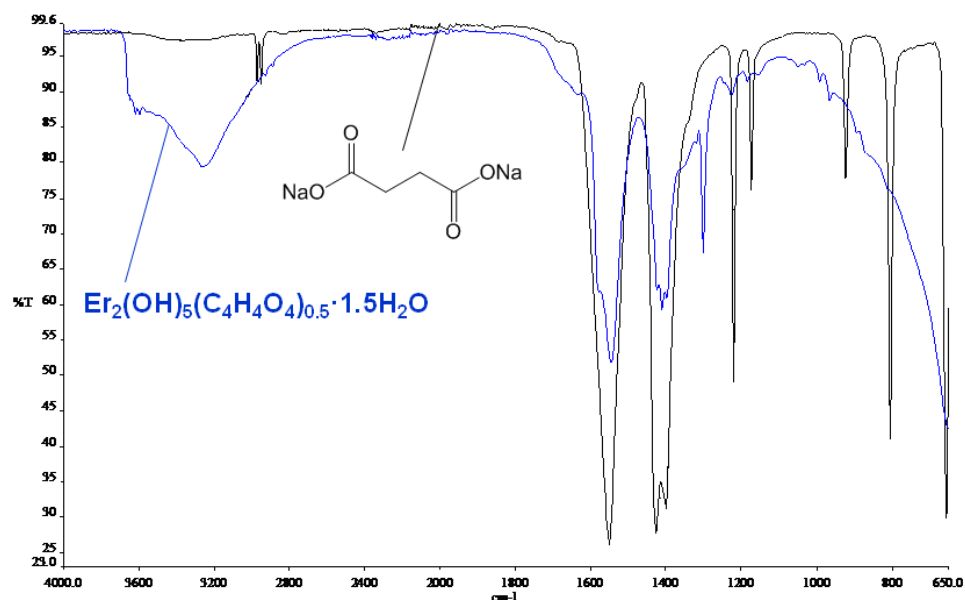


Figure 11 FTIR spectrum of $\text{Er}_2(\text{OH})_5(\text{C}_4\text{H}_4\text{O}_4)_{0.5}\cdot 1.5\text{H}_2\text{O}$ (shown in blue) and succinic acid disodium salt $\text{C}_4\text{H}_4\text{O}_4\text{Na}_2$ (shown in black).

The data herein confirms that these are a family of highly flexible intercalation hosts, being able to accommodate small anions with a decrease in the interlayer separation and large surfactant anions where there is up to a threefold increase in the interlayer separation relative to the host. Additional characterisation by TGA indicates that the thermal behavior of these intercalation compounds is similar to that of comparable organic derivatives of LDHs. Depending on the nature of the organic anion, the TGA traces comprise two or three distinct regions of mass loss. Figure 12 shows the TGA trace for $\text{Er}_2(\text{OH})_5(\text{C}_4\text{H}_4\text{O}_4)_{0.5}\cdot 1.5\text{H}_2\text{O}$, displaying a total mass loss of 23.72 % with total decomposition to Er_2O_3 by 900 °C, as confirmed by X-ray diffraction (calculated mass loss 24.32 %).

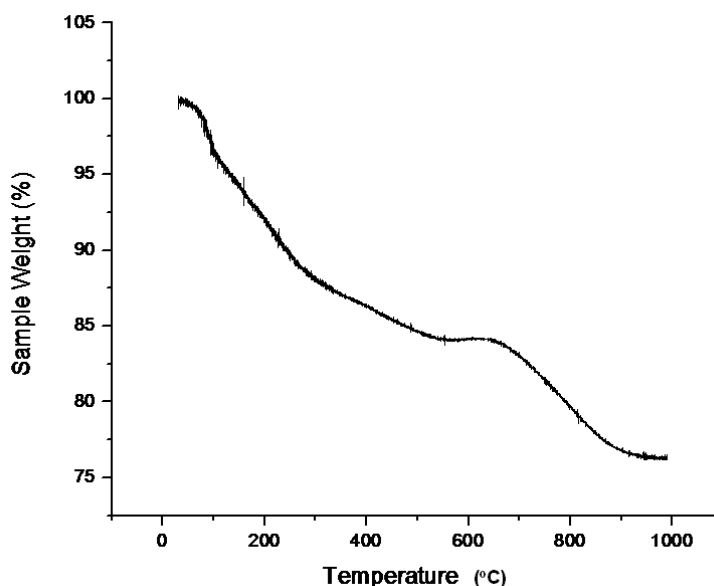


Figure 12 TGA trace for $\text{Er}_2(\text{OH})_5(\text{C}_4\text{H}_4\text{O}_4)_{0.5}\cdot 1.5\text{H}_2\text{O}$ showing total mass loss of 23.72 % by 900 °C.

The ease of anion exchange in the $\text{Ln}_2(\text{OH})_5\text{NO}_3\cdot 1.5\text{H}_2\text{O}$ materials contrasts with the more forcing conditions of prolonged heating at 65 °C required to bring about complete anion exchange for $\text{La}(\text{OH})_2\text{NO}_3\cdot \text{H}_2\text{O}$.⁷ It is likely that this difference reflects differing nitrate environments in the two host lattices. In $\text{La}(\text{OH})_2\text{NO}_3\cdot \text{H}_2\text{O}$ the nitrate anion is directly coordinated to the La^{3+} cation and by analogy to the $[\text{Ln}_4(\text{OH})_{10}(\text{H}_2\text{O})_4]\text{A}$ ($\text{Ln} = \text{Y}, \text{Dy}, \text{Ho}, \text{Yb}$; $\text{A} = 2,6\text{-naphthalenedisulfonate}, 2,6\text{-anthraquinonedisulfonate}$) phases it is likely that in the host materials reported here the nitrate is uncoordinated in the interlayer gallery permitting more facile exchange reactions. This rationale is supported by the FTIR data (Figure 9) which confirms the

presence of free nitrate anions. A comparison of the interlayer separations of the terephthalate intercalates of both families (12.9 Å for $\text{La}(\text{OH})_2(p\text{-C}_8\text{H}_4\text{O}_4)_{0.5}\cdot\text{H}_2\text{O}$ and 13.1 Å for $\text{Er}_2(\text{OH})_5(p\text{-C}_8\text{H}_4\text{O}_4)_{0.5}\cdot\text{H}_2\text{O}$) indicates that the layer thickness is comparable in the different host lattices with the slightly smaller value observed for $\text{La}(\text{OH})_2(p\text{-C}_8\text{H}_4\text{O}_4)_{0.5}\cdot\text{H}_2\text{O}$, consistent with the coordination of the anion to the La^{3+} cation in that system.

2.2.3 Orientation of the Guest Anions

From an analysis of the interlayer separations of the aliphatic dicarboxylate intercalates ($\text{Ln}_2(\text{OH})_5(\text{OOC}(\text{CH}_2)_n\text{COO})_{0.5}\cdot 1.5\text{H}_2\text{O}$; $n = 0 - 6$) it is possible to infer the orientation of the guest anions between the layers, these are summarized in Table 3. The plot of interlayer separation against the number of CH_2 groups in the chain, n , for the Er compounds is shown in Figure 14a and indicates a roughly linear relationship between the gallery height and the chain length. The gradient of the plot is $1.07 \text{ \AA}/\text{C atom}$ which can be compared with the linear intercarbon distance along the chain of 1.27 \AA (Figure 13) indicating the formation of a monolayer of anions in the interlayer gallery and allowing a tilting angle of 58° to be calculated. The tilt angles decrease across the series varying from 82° for Tb to 51° for the Tm host.

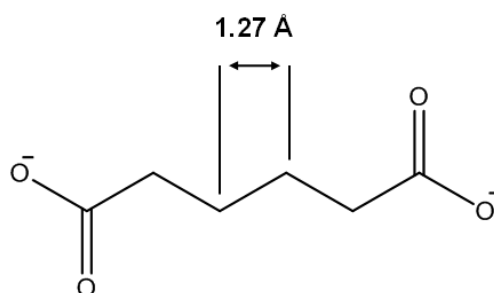


Figure 13 Schematic diagram to show the linear intercarbon distance along the aliphatic carboxylate chain of 1.27 \AA .

From the schematic orientation shown in Figure 14b it can be seen that this orientation is likely to maximize the electrostatic interactions between the host layers

and the guest anions and these tilt angles are comparable to those seen in similar LDH systems.^{17, 18}

Table 3 Orientation angles of a monolayer of anions within the interlayer gallery for $\text{Ln}(\text{OH})_5\text{NO}_3 \cdot 1.5\text{H}_2\text{O}$ materials (Y, Tb – Tm).

Ln	Orientation Angle (°)
Y	64
Tb	82
Dy	64
Ho	62
Er	58
Tm	51

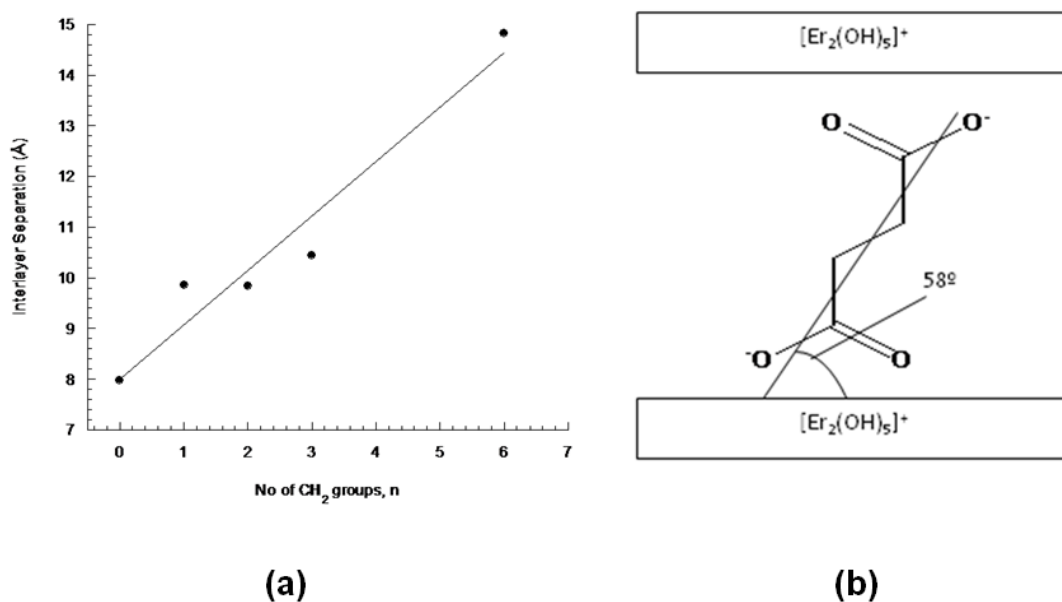


Figure 14 (a) Plot of interlayer separation against number of CH₂ groups, n , in the aliphatic chain of some dicarboxylate intercalates, $\text{Er}_2(\text{OH})_5(\text{OOC}(\text{CH}_2)_n\text{COO})_{0.5} \cdot 1.5\text{H}_2\text{O}$.

(b) Schematic representation of the succinate intercalate of $\text{Er}_2(\text{OH})_5\text{NO}_3 \cdot 1.5\text{H}_2\text{O}$ indicating the orientation of the guest anions between the layers.

2.2.4 Comparison with other LRH materials

Anion exchange reactions have also been performed with 2,6-naphthalenedisulfonate (NDS) and 2,6-anthraquinonedisulfonate (AQDS) in order to permit a comparison with the phases reported by Gándara *et al.* These anion exchange reactions, with the Y and Er host lattices, proved to be incomplete in the majority of cases with significant amounts of N being detected in the elemental analysis. XRD data showed that the products consist of unreacted host lattice and an expanded phase with interlayer separations of around 15.6 Å for the NDS materials and 18.2 Å for the AQDS phases compared with the published values of 15.26 Å and 17.83 Å respectively. In both cases the anion exchange materials have interlayer separations which are slightly larger than those prepared hydrothermally by Gándara *et al.* It is likely that these differences result from variations in the orientation of the guest anion due to differences in the degree of hydration rather than from significant differences in the layer structure which retains the composition $[\text{Ln}_2(\text{OH})_5]^+$ after exchange. In order to confirm this, the materials were also synthesised following the method reported by Gandara *et al.* giving rise to phases with the same interlayer separation as those prepared by anion exchange. Powder XRD data for $\text{Y}_2(\text{OH})_5(\text{NDS})_{0.5} \cdot x\text{H}_2\text{O}$ prepared hydrothermally and by anion exchange are shown for comparison in Figure 15 from which it is clear that the same material is prepared via both routes and that the hydrothermal synthesis is a more efficient route to these particular compounds.

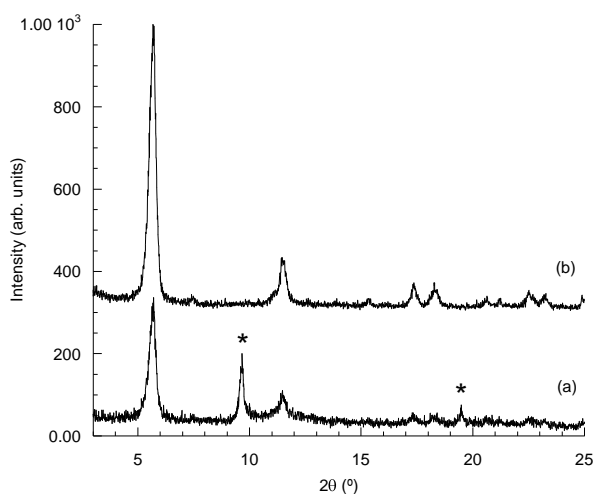


Figure 15 Powder XRD diffraction patterns of $\text{Y}_2(\text{OH})_5(\text{NDS})_{0.5} \cdot x\text{H}_2\text{O}^\dagger$ prepared

(a) by anion exchange and

(b) hydrothermally

(* indicates unreacted $\text{Y}_2(\text{OH})_5\text{NO}_3 \cdot 1.5\text{H}_2\text{O}$ in the anion exchange sample). † Reactions carried out by Miss L. K. Jackson.

2.3 Properties of the $\text{Ln}_2(\text{OH})_5\text{NO}_3 \cdot 1.5\text{H}_2\text{O}$ Materials

2.3.1 Competitive Anion Exchange Reactions

Layered double hydroxides have been reported to exhibit high anion exchange selectivity between isomeric pairs and applications of these materials in the field of separation science were reviewed in section 1.6.2.

$[\text{LiAl}_2(\text{OH})_6]\text{Cl} \cdot \text{H}_2\text{O}$ demonstrates a 98 % selectivity for fumarate ($\text{trans-C}_4\text{H}_2\text{O}_4^{2-}$) from equimolar mixtures of fumarate and maleate and a 95 % selectivity for terephthalate ($1,4\text{-C}_8\text{H}_4\text{O}_4^{2-}$) from a mixture of 1,2-, 1,3- and 1,4-isomers.¹⁹ The material also displays up to 99 % selectivity for 1,5-naphthalenedisulfonate over 2,6-naphthalenedisulfonate dependant on temperature and solvent system.²⁰ In addition the material has been shown to be highly selective for chlorophenoxyacetates,

nitrophenolates and functionalized benzoates.²¹⁻²³ Layered double hydroxides of the type $[\text{MAl}_4(\text{OH})_{12}](\text{NO}_3)_2 \cdot y\text{H}_2\text{O}$ ($\text{M} = \text{Zn, Ni, Co}$) also preferentially uptake *para*- $\text{C}_8\text{H}_4\text{O}_4^{2-}$, 2-naphthalenesulfonate and 1,5-naphthalenedisulfonate at levels of up to 93 % according to reaction conditions²⁴ whilst $\text{Ca}_2\text{Al}(\text{OH})_6 \cdot \text{NO}_3 \cdot 2\text{H}_2\text{O}$ selectively intercalates 95 % *para*- $\text{C}_8\text{H}_4\text{O}_4$.²⁵

Selectivity reactions for $\text{Ln}_2(\text{OH})_5\text{NO}_3 \cdot 1.5\text{H}_2\text{O}$ ($\text{Ln} = \text{Tb} - \text{Tm}$) were carried out overnight at room temperature with an equimolar solution of fumarate / maleate and phthalate / terephthalate, the results are summarized below in Table 4. These anions were chosen as they have been shown to intercalate successfully into these lanthanide hydroxynitrate materials (section 2.2.2). 1,4-benzenedicarboxylate in particular is important in the synthesis of polyester but is derived from crude oil as a mixture and so to this end an effective means of separation is vital. The intercalated dicarboxylate anions were removed from the host by means of a secondary reaction with Na_2CO_3 at room temperature overnight in D_2O . The solid product was removed by vacuum filtration and the filtrate analysed by ^1H NMR. Powder XRD was carried out on the solid obtained from the secondary reaction in order to confirm complete exchange.

Reaction monitoring by means of *in situ* energy dispersive X-ray diffraction was attempted but prevented by the speed of reaction, even when dropwise addition via a syringe pump was used, with exchange complete within 1-2 minutes. Thus insight into the kinetic and mechanistic pathways of these reactions unfortunately is not possible.

Table 4 Selectivity results for $\text{Ln}_2(\text{OH})_5\text{NO}_3 \cdot 1.5\text{H}_2\text{O}$ ($\text{Ln} = \text{Tb} - \text{Tm}$) materials.

$\text{Ln}_2(\text{OH})_5\text{NO}_3 \cdot 1.5\text{H}_2\text{O}$	Isomer Pairs	Interlayer Separation (Å)	Selectivity (%)
Tb	<i>cis-</i> / <i>trans</i> - $\text{C}_4\text{H}_2\text{O}_4^{2-}$	9.6	No exchange ^a
	<i>ortho-</i> / <i>para</i> - $\text{C}_8\text{H}_4\text{O}_4^{2-}$	12.8	56 % / 44 %
Dy	<i>cis-</i> / <i>trans</i> - $\text{C}_4\text{H}_2\text{O}_4^{2-}$	9.6	89 % / 11 %
	<i>ortho-</i> / <i>para</i> - $\text{C}_8\text{H}_4\text{O}_4^{2-}$	12.4	64 % / 36 %
Ho	<i>cis-</i> / <i>trans</i> - $\text{C}_4\text{H}_2\text{O}_4^{2-}$	9.6	86 % / 14 %
	<i>ortho-</i> / <i>para</i> - $\text{C}_8\text{H}_4\text{O}_4^{2-}$	13.4	64 % / 36 %
Er	<i>cis-</i> / <i>trans</i> - $\text{C}_4\text{H}_2\text{O}_4^{2-}$	9.9	87 % / 13%
	<i>ortho-</i> / <i>para</i> - $\text{C}_8\text{H}_4\text{O}_4^{2-}$	13.2	77 % / 23 %
Tm	<i>cis-</i> / <i>trans</i> - $\text{C}_4\text{H}_2\text{O}_4^{2-}$	10.0	84 % / 16 %
	<i>ortho-</i> / <i>para</i> - $\text{C}_8\text{H}_4\text{O}_4^{2-}$	13.6	75 % / 25 %

^a Secondary exchange reaction with Na_2CO_3 in D_2O proved unsuccessful.

The data shows that *cis*- $\text{C}_4\text{H}_2\text{O}_4^{2-}$ and *ortho*- $\text{C}_8\text{H}_4\text{O}_4^{2-}$ are selectively intercalated consistently over the range of $\text{Ln}_2(\text{OH})_5\text{NO}_3 \cdot 1.5\text{H}_2\text{O}$ host lattices studied. Preference for *cis*- $\text{C}_4\text{H}_2\text{O}_4$ is higher than that for *ortho*- $\text{C}_8\text{H}_4\text{O}_4$ for these materials.

For *cis*- and *trans*- $\text{C}_4\text{H}_2\text{O}_4^{2-}$ mixtures, the *cis* isomer is preferentially intercalated in excesses of between 84-89 %, with the highest selectivity observed for the Dy material. It was not possible to obtain a value for the *cis* / *trans* selectivity of the Tb material as secondary reaction with Na_2CO_3 was unsuccessful. For *ortho*- and *para*- $\text{C}_8\text{H}_4\text{O}_4$ mixtures results were less consistently high but *ortho*- $\text{C}_8\text{H}_4\text{O}_4^{2-}$ was always intercalated at levels of 56-77 %, with the highest value obtained by the Er material.

The highest preference for *cis*-C₄H₂O₄²⁻ is displayed by Dy₂(OH)₅NO₃·1.5H₂O. From an equimolar *cis* / *trans* mixture 89 % *cis*-C₄H₂O₄²⁻ selectively intercalates giving a d-spacing of 9.6 Å. For singular reactions with *cis* and *trans* isomers d-spacings of 11.3 Å and 9.6 Å are obtained respectively (Figure 16). From the X-ray diffraction pattern alone it could be inferred that there is a preference for fumarate, however the ¹H NMR below shows that this is not the case.

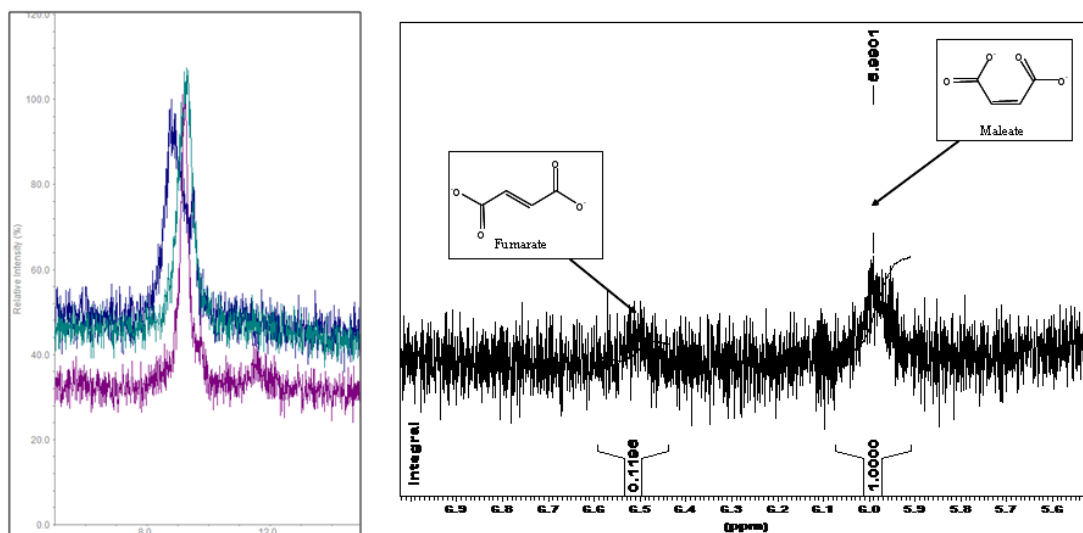


Figure 16 (a) Powder XRD diffraction patterns of:

- (i) Dy₂(OH)₅(*cis*-C₄H₂O₄)_{0.5}·1.5H₂O,
 - (ii) Dy₂(OH)₅(*trans*-C₄H₂O₄)_{0.5}·1.5H₂O and
 - (iii) Dy₂(OH)₅(*cis*-C₄H₂O₄)_{0.445}(*trans*-C₄H₂O₄)_{0.055}·1.5H₂O.
- (b) ¹H NMR spectrum following secondary exchange reaction.

For *ortho*- and *para*-C₈H₄O₄ reactions, the highest selectivity is displayed by the Er material. Er₂(OH)₅NO₃·1.5H₂O uptakes 77 % *ortho*-C₈H₄O₄²⁻ resulting in an interlayer separation of 13.2 Å. For the individual reactions with *ortho* and *para* isomers d-spacings of 14.0 Å and 13.1 Å are obtained. Here also, the interlayer separations for the materials indicate a preference opposite to that confirmed by ¹H NMR, as shown by Figure 17.

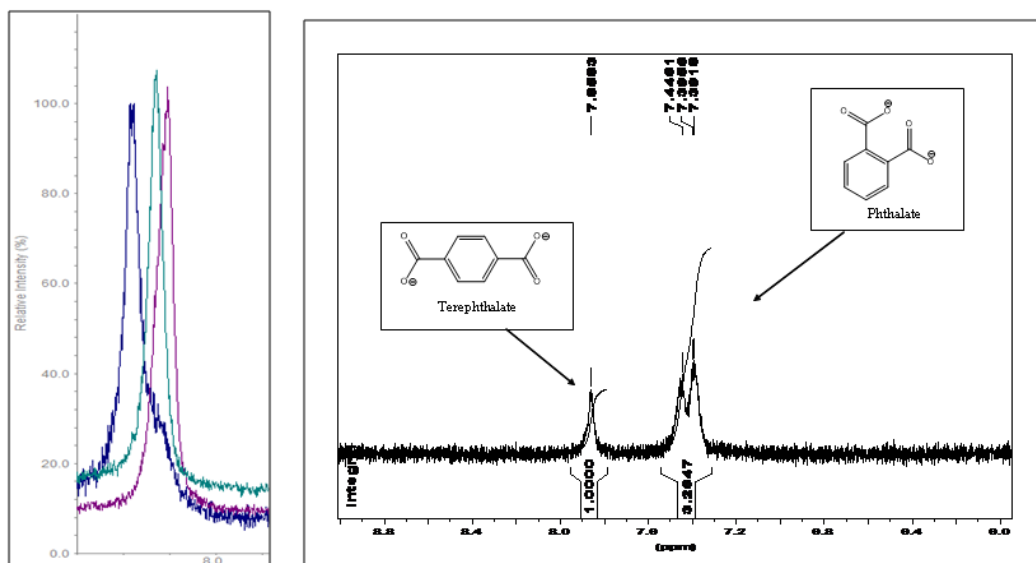


Figure 17 (a) Powder XRD diffraction patterns of:

- (i) Er₂(OH)₅(*ortho*-C₈H₄O₄)_{0.5}·1.5H₂O,
 - (ii) Er₂(OH)₅(*para*-C₈H₄O₄)_{0.5}·1.5H₂O and
 - (iii) Er₂(OH)₅(*ortho*-C₈H₄O₄)_{0.385}(*para*-C₈H₄O₄)_{0.115}·1.5H₂O.
- (b) ¹H NMR spectrum following secondary exchange reaction.

These observations are in stark contrast with previous selectivity studies where completely opposing preferences have been shown, [LiAl₂(OH)₆]Cl·H₂O¹⁹ demonstrates a 98 % selectivity for *trans*-C₄H₂O₄²⁻ and 95 % for *para*-C₈H₄O₄²⁻. [MAl₄(OH)₁₂](NO₃)₂·γH₂O (M = Zn, Cu, Ni, Co) and Ca₂Al(OH)₆·NO₃·2H₂O materials also express preferences for terephthalate in excesses of 90 %.^{24, 25}

Several factors are thought to be significant in intercalation reactions; these include the favorability of host-guest electrostatic interactions and the magnitude of packing energies of the intercalated anions (guest-guest interactions) which are chiefly governed by the ability to form hydrogen bonds or π-π stack in the case of aromatic

systems. It is also likely that the solvation factors of the initial and final guests are important. The effects of initial and final guest enthalpies of solvation will be discounted as possible factors in the unusual selectivity displayed here. These anions have been used in previous studies of LDHs with interlayer nitrate where opposite preferences were observed.^{24, 25} It has also been postulated that the ordering of the metal cations, the charge density or specific metal content within the layer impart selectivity properties on LDHs.²⁰ It is clear from the literature that selective intercalation is a thermodynamic phenomenon. A number of reports where EDXRD is employed as a means of monitoring selectivity reactions note that either following initial uptake of two isomers, the least favourable is de-intercalated¹⁹ or initially a kinetic product and then a thermodynamic product forms.^{25, 26} An increase in reaction time to 48 hours with these materials gave no change in selectivity preferences, suggesting that therefore these reactions are proceeding under thermodynamic control.

The reasons for the high preferential intercalation of fumarate and terephthalate have previously been cited as resulting from increased host-guest interactions.²⁴ Electrostatic interactions are maximised by the ability of fumarate and terephthalate to bridge across two hydroxide layers and π - π stacking interactions are thought to be maximised for *para*-C₈H₄O₄ in this configuration. More information concerning host-guest hydrogen bonding interactions is revealed by careful structural inspection.

[LiAl₂(OH)₆]Cl·H₂O displays high selectivity for *trans*-C₄H₂O₄ and *para*-C₈H₄O₄, its layer structure is shown in Figure 18a. The structure consists of a regular repeating corrugated surface. In terms of hydrogen bonding, the most significant bond distances are those between two adjacent hydroxides from the same layer plane. For this material this corresponds to O-O distances of 3.15 Å and H-H distances of 2.89 Å. This regular spacing of O-H groups and the O-O spacing of 3.15 Å matches well with the geometry of incoming carboxylate groups of both fumarate and maleate anions. This spatial arrangement enables both oxygens from a single carboxylate CO₂⁻ functionality to engage in hydrogen bonding with adjacent O-H groups, forming a thermodynamically favored structure (see Figure 18b). However, whilst the fumarate anions are able to form complementary H-bonding interactions with a second layer, resulting in strong host-guest interactions, maleate is not. This is likely to be the reason for the high preference displayed by this material for this anion.

Similarly, it is likely that the preference for terephthalate can be accounted for on this basis, as Figure 18c shows. A further schematic of typical hydrogen-bonding interactions between the metal hydroxide layer and terephthalate and phthalate anions is given in Figure 19.

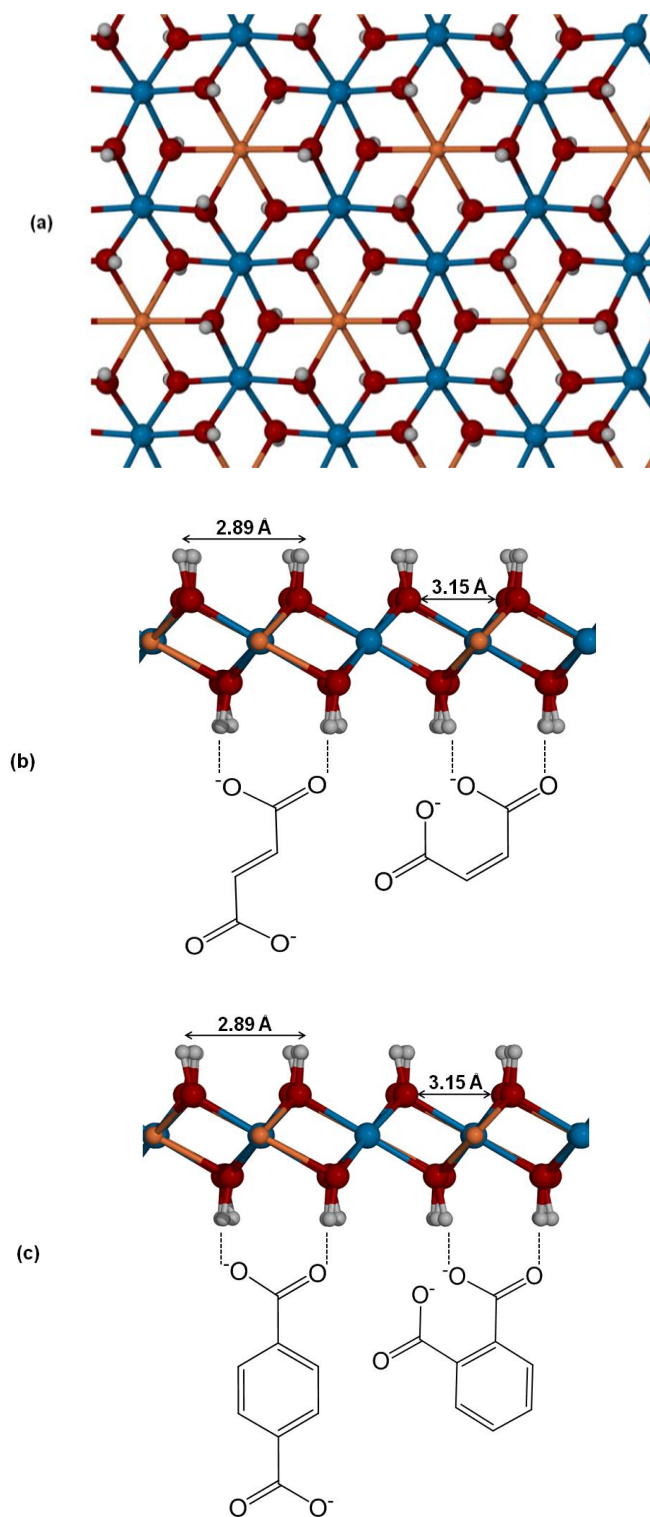


Figure 18 (a) View down [001] direction of $[\text{LiAl}_2(\text{OH})_6]\text{Cl}\cdot\text{H}_2\text{O}$, (b) layer interactions with fumarate and maleate and (c) layer interactions with terephthalate and phthalate.

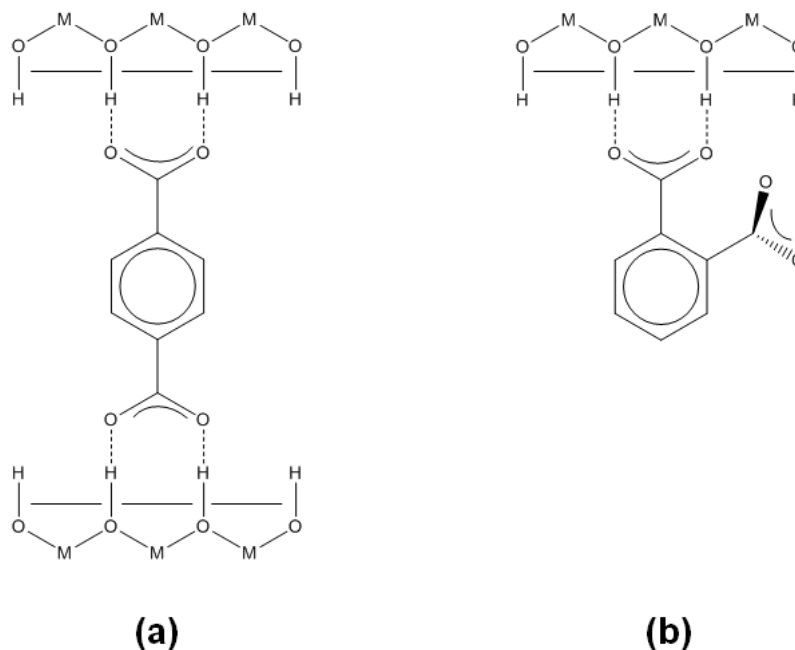


Figure 19 Schematic of hydrogen-bonding interactions between (a) terephthalate anion and (b) phthalate anion and the metal hydroxide layer.

Whilst the structure of the $\text{Ln}_2(\text{OH})_5\text{NO}_3 \cdot 1.5\text{H}_2\text{O}$ (Tb - Tm) materials is unknown, it is likely that the unusual selectivity preferences displayed are linked to the layer structure. Given that both *cis*- $\text{C}_4\text{H}_2\text{O}_4^{2-}$ and *ortho*- $\text{C}_8\text{H}_4\text{O}_4^{2-}$ are selectively intercalated, it is suggested that the carboxylate groups of these isomers are configured as to provide favourable interactions with the lanthanide hydroxide layers.

The closely related structure of Y-2,6-naphthalenedisulfonate (YNDS) is shown in Figure 20.¹¹ The structure consists of $[\text{Y}_4(\text{OH})_{10}(\text{H}_2\text{O})_4]^{2+}$ cationic layers formed by eight- and nine-coordinated rare-earth atoms linked through μ_3 -hydroxy groups and one water molecule to give two different coordination polyhedra; a dodecahedron and a monocapped square antiprism.

Closer examination of the hydrogen-bonding interactions with the organic guest (Figure 20 inset) reveals that the coordinated water molecules project further into the interlayer gallery than the hydroxides. This gives two hydrogen bond donor sites at different “heights” from the 2D layer. Each of the sulfonate groups from NDS^{2-} forms a hydrogen-bonding interaction with a hydroxide group and an adjacent water

molecule. One of the sulfonate oxygens clearly approaches closer to the yttrium hydroxide layer to enable the close contact to the hydroxide proton required for hydrogen bonding. This results in the anion binding in a non-perpendicular fashion to the 2D layer, as evidenced by the tilting angle observed by Gandara *et al.* of 37.80°. This contrasts with the orientation of guest anions observed for $[\text{LiAl}_2(\text{OH})_6]\text{Cl}\cdot\text{H}_2\text{O}$ of approximately 90° relative to the hydroxide layer.¹⁸ Clearly this indicates a significant difference in the host-guest interactions between these materials thus affecting their selectivity preferences.

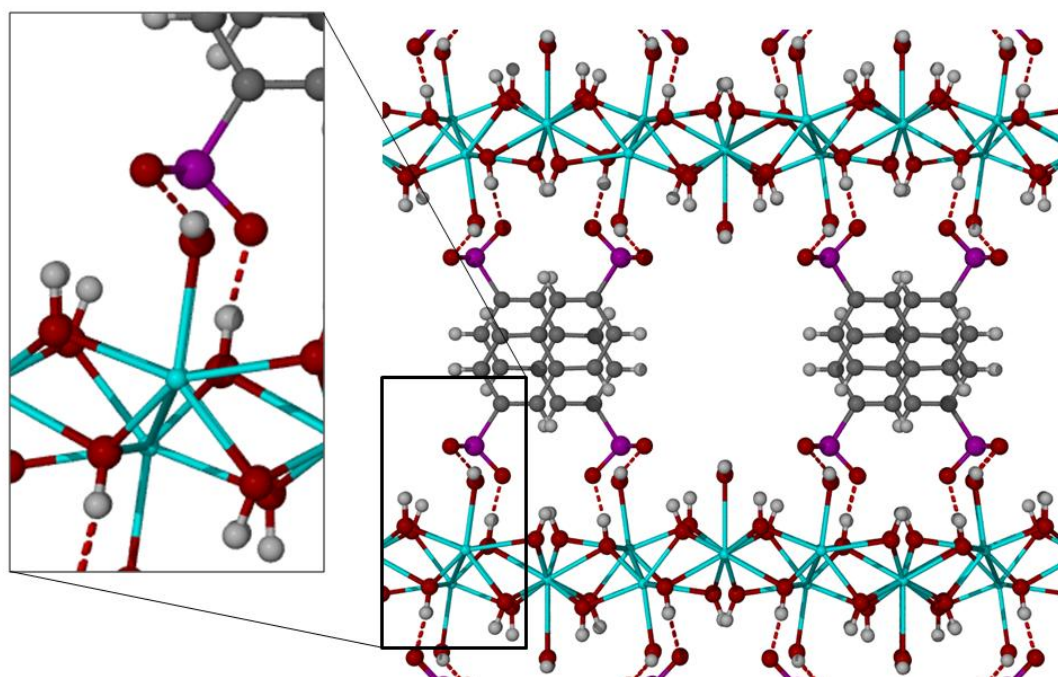


Figure 20 Crystal structure of YNDS, with shortest hydrogen-bonding interactions shown as dashed bonds. INSET: Expansion of H-bonding interactions between sulfonate and adjacent hydroxide and water molecule.

For $\text{Ln}_2(\text{OH})_5\text{NO}_3\cdot 1.5\text{H}_2\text{O}$ ($\text{Ln} = \text{Tb} - \text{Tm}$) materials, selectivity results show that *cis*- $\text{C}_4\text{H}_2\text{O}_4^{2-}$ and *ortho*- $\text{C}_8\text{H}_4\text{O}_4^{2-}$ are preferentially intercalated consistently over the range of $\text{Ln}_2(\text{OH})_5\text{NO}_3\cdot 1.5\text{H}_2\text{O}$ host lattices studied. This can be attributed to this different orientation angle arising from the presence of the protruding water molecule which in turn causes an irregular hydrogen bonding surface. Analogously to the NDS^{2-} interaction, the carboxylate anions would also be expected to be significantly tilted with respect to the layer (assuming CO_2^- also interacts with adjacent hydroxide groups and water molecules of the layer). This, it is suggested, would enable the

maleate / phthalate anions to project both carboxylate groups towards the same layer face, allowing both to be involved in hydrogen bonding and thus maximize electrostatic interactions. This is a possible explanation for the preferences displayed by these materials for these isomers.

It is important to note that the arrangement of the lanthanide hydroxide layers does not preclude the binding of fumarate or terephthalate. Clearly the carboxylate groups for each are also able to bind in the same sites as the opposing isomers, with fumarate and terephthalate bridging across hydroxide layers. Therefore the binding of both isomers is energetically similar overall, consistent with the mixed levels of selectivity observed (56 – 89 %).

Analysis of crystal structures containing maleate and phthalate reveals more information concerning hydrogen bonding interactions. Figure 21a shows the crystal structure of *bis*(2-aminopyridinium)maleate.²⁷ Here the two carboxylate groups are twisted relative to one another and form interactions at two different “heights”. The crystal structure of *bis* 2-amino-3 methylpyridinium is shown in Figure 21b.²⁸ Again the carboxylate groups are staggered however here the height differences between the two are less pronounced.

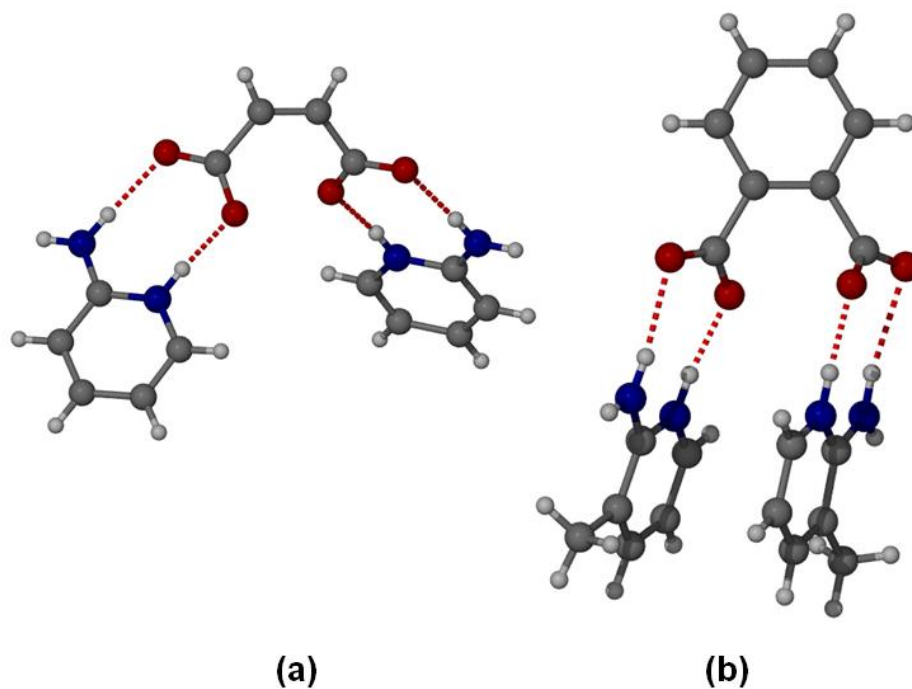


Figure 21 Crystal structures of (a) *bis*(2-aminopyridinium)maleate²⁷ and (b) *bis* 2-amino-3 methylpyridinium.²⁸

The difference in “heights” observed here may account for the higher preference for *cis*-C₄H₂O₄ (84 – 89 %) than for *ortho*-C₈H₄O₄ (56 – 77 %) of these materials.

A schematic of the likely interactions of the maleate and phthalate anions with the [Y₄(OH)₁₀(H₂O)₄]²⁺ layer is shown in Figure 22. It can be envisaged that the alternating arrangement of interlayer hydroxides and coordinated water molecules, also likely to be encountered in Ln₂(OH)₅NO₃·1.5H₂O (Ln = Tb – Tm) materials provides a suitable face to which the anions can bind.

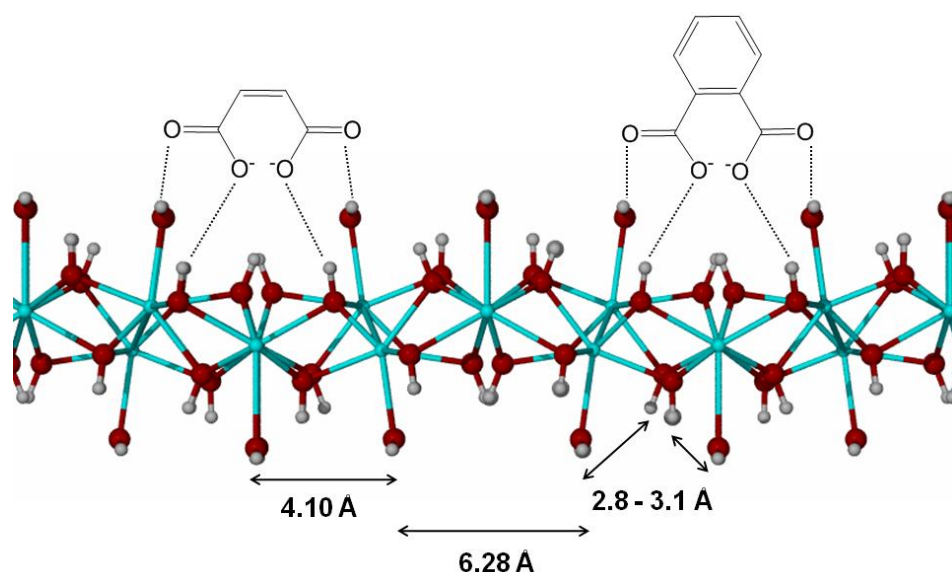


Figure 22 The likely interactions of maleate and fumarate anions with the [Y₄(OH)₁₀(H₂O)₄]²⁺ layer.

Since these isomers are not able to bridge across the hydroxide layers owing to the configuration, it is most likely that the anions form two layers in the interlayer gallery. The material which displays the highest selectivity for *o*-C₈H₄O₄²⁻ is Er₂(OH)₅(NO₃)_{0.5}·1.5H₂O (89 %). The bilayer arrangement of Er₂(OH)₅(*o*-C₈H₄O₄)_{0.5}·H₂O is reflected in the correspondingly higher basal spacing observed for the singular reaction with *o*-C₈H₄O₄²⁻ (d = 14.0 Å) compared with d = 13.1 Å obtained from reaction with *p*-C₈H₄O₄²⁻. Similarly, for the material which displays the highest selectivity for *cis*-C₄H₂O₄²⁻ (Dy₂(OH)₅(NO₃)_{0.5}·1.5H₂O at 77 %) the likely bilayer arrangement of the *cis*-intercalate is supported by the observed larger d-spacing of 11.3 Å, as opposed to 9.6 Å for Dy₂(OH)₅(*trans*-C₄H₂O₄)_{0.5}·H₂O.

2.3.2 Optical Properties

Luminescence is defined as the decay from an electronically excited state by photon emission. There are two types of luminescence; fluorescence which is spin-allowed with lifetimes in the region $10^{-6} - 10^{-12}$ s and phosphorescence which is spin-forbidden and requires a change in spin multiplicity. Phosphorescence lifetimes are longer and typically exceed 10^{-6} s and may last a number of seconds. Lanthanide luminescence in the solid state gives sharp emission lines e.g., Eu^{3+} is red and Tb^{3+} is green. This luminescence is weak and so an “antenna” molecule is often used to facilitate energy transfer. It is important to note that luminescence can only occur provided non-radiative processes do not take over.

The ultra-violet absorption spectrum of $\text{Tb}_2(\text{OH})_5\text{NO}_3 \cdot 1.5\text{H}_2\text{O}$ and $\text{Tb}_2(\text{OH})_5\text{AQDS} \cdot 3\text{H}_2\text{O}$ are shown in Figure 23. The spectra show bands at 220 and 300 nm with a number of weaker absorptions in the region 350 – 490 nm for the host material and peaks at 215, 265 and 340 nm for the AQDS intercalate.

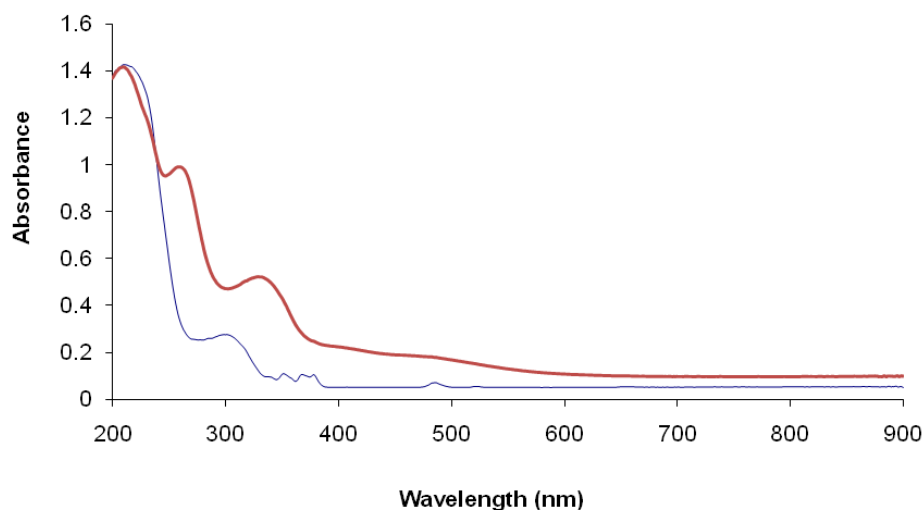


Figure 23 Ultra-violet absorption spectra of $\text{Tb}_2(\text{OH})_5\text{NO}_3 \cdot 1.5\text{H}_2\text{O}$ (shown in blue) and $\text{Tb}_2(\text{OH})_5(\text{AQDS})_{0.5} \cdot 3\text{H}_2\text{O}$ (shown in red).

Emission spectra for $\text{Tb}_2(\text{OH})_5\text{NO}_3 \cdot 1.5\text{H}_2\text{O}$ were measured by selective excitation at 220 and 370 nm with greatest luminescent intensity achieved by excitation at 370 nm. The corresponding solid state emission spectrum is shown in Figure 24. The four bands, observed at 490, 545, 585 and 620 nm, correspond to the characteristic green emission from the ${}^5\text{D}_4 \longrightarrow {}^7\text{F}_j$ ($j = 6, 5, 4, 3$) transitions of Tb^{3+} .²⁹ The lifetime however was found to be disappointingly low at 0.038 ms ($\text{Tb}^{3+}(\text{aq}) = 3.8$ ms).³⁰

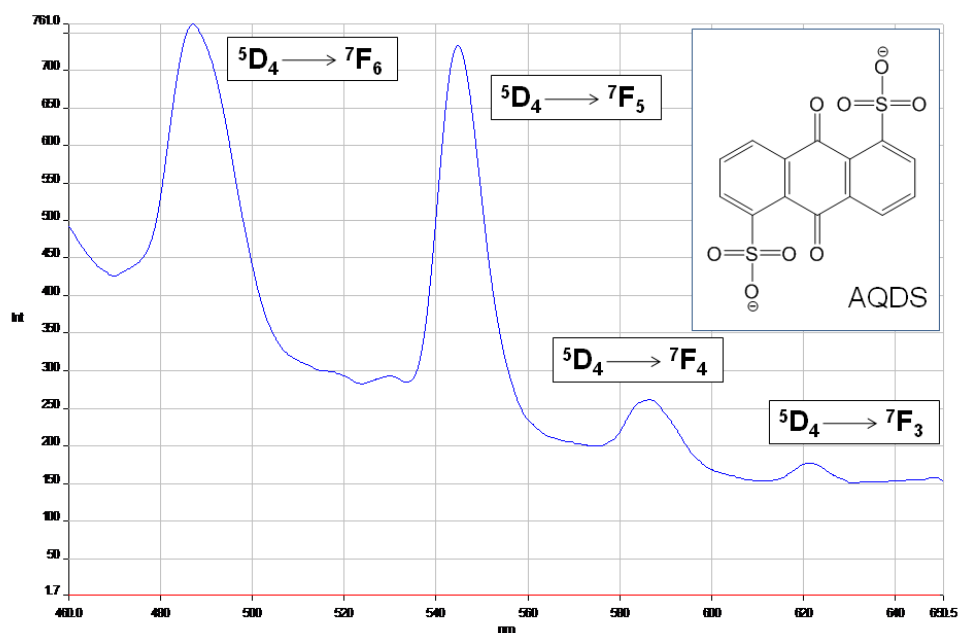


Figure 24 Emission spectrum of $\text{Tb}_2(\text{OH})_5\text{NO}_3 \cdot 1.5\text{H}_2\text{O}$ (shown in blue) and $\text{Tb}_2(\text{OH})_5(\text{AQDS})_{0.5} \cdot 3\text{H}_2\text{O}$ (shown in red). $\lambda_{\text{ex}} = 370$ nm. INSET: structure of AQDS.

The energy gap between the lowest emissive state and the highest non-emissive state for Tb^{3+} is $14\,800\text{ cm}^{-1}$.³⁰ This energy gap can be bridged by weak vibronic coupling of the excited state with high frequency oscillators such as the $\nu(\text{O-H})$ vibration of coordinated H_2O molecules and indeed the coordinated hydroxide anions, such as those present in the $\text{Ln}_2(\text{OH})_5\text{NO}_3 \cdot 1.5\text{H}_2\text{O}$ materials.

The photoluminescence of lanthanide cations is known to be sensitive to the presence of water molecules and hydroxide anions.^{31, 32} In the case of Tb^{3+} the energy gap is conveniently bridged by four quanta of O-H vibrational energy, this is the most probable explanation for the poor lifetime observed for this material (Figure 25a).³³ This efficient non-radiative relaxation has also been observed to quench ${}^5\text{D}_0$ emission

for the microporous rare earth dicarboxylate $[\text{Eu}_{0.01}\text{Gd}_{0.99}(\text{H}_2\text{O})_2][\text{O}_2\text{C}(\text{CH}_2)_3\text{CO}_2]_3 \cdot 4\text{H}_2\text{O}$.³⁴

In an effort to increase the observed lifetime it was decided to manipulate a phenomenon known as sensitized luminescence. By exciting via a conjugated organic ligand it is possible to obtain fast intramolecular energy transfer to give lanthanide emission, as shown in Figure 25b.

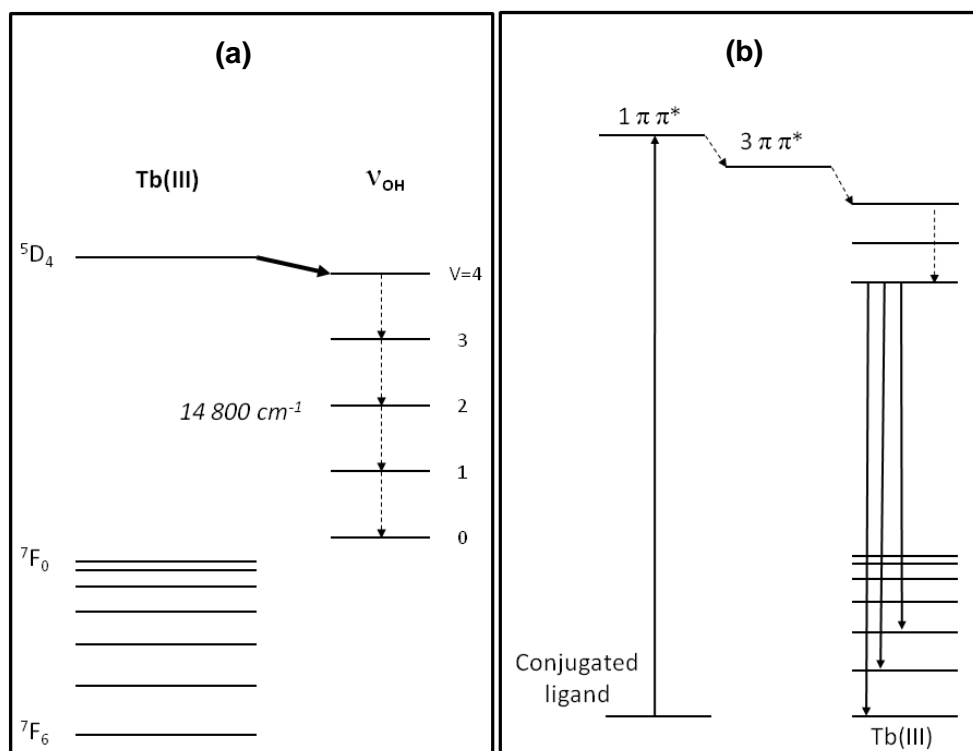


Figure 25 Energy level diagram for Tb^{3+} luminescence (a) quenched by $\nu(\text{O-H})$ and (b) sensitized luminescence (adapted from *Chemistry of the f-block Elements*, Gordon and Breach Science Publishers, Singapore, 2001).³³

A wide range of organic molecules have been employed as sensitizers, these have been primarily studied in the field of luminescent metal organic frameworks.³⁵ Conjugated organics with extended π systems are often strongly absorbing and emissive.

It was for this reason AQDS was chosen as a suitable candidate, in addition intercalation into $\text{Tb}_2(\text{OH})_5\text{NO}_3 \cdot 1.5\text{H}_2\text{O}$ has also been shown previously to be successful. However, surprisingly it was found to completely quench emission, with no emission observed from this material (Figure 24).

The ultra-violet absorption spectrum of $\text{Dy}_2(\text{OH})_5\text{NO}_3 \cdot 1.5\text{H}_2\text{O}$ and $\text{Dy}_2(\text{OH})_5\text{AQDS} \cdot 3\text{H}_2\text{O}$ are shown in Figure 26. The spectrum for the host material shows bands at 220 and 300 nm with a number of weaker absorptions in the region 350 – 480 nm and 750 – 900 nm. The AQDS intercalate spectrum has peaks at 220, 260 and 340 nm and also in the region 750 – 900 nm.

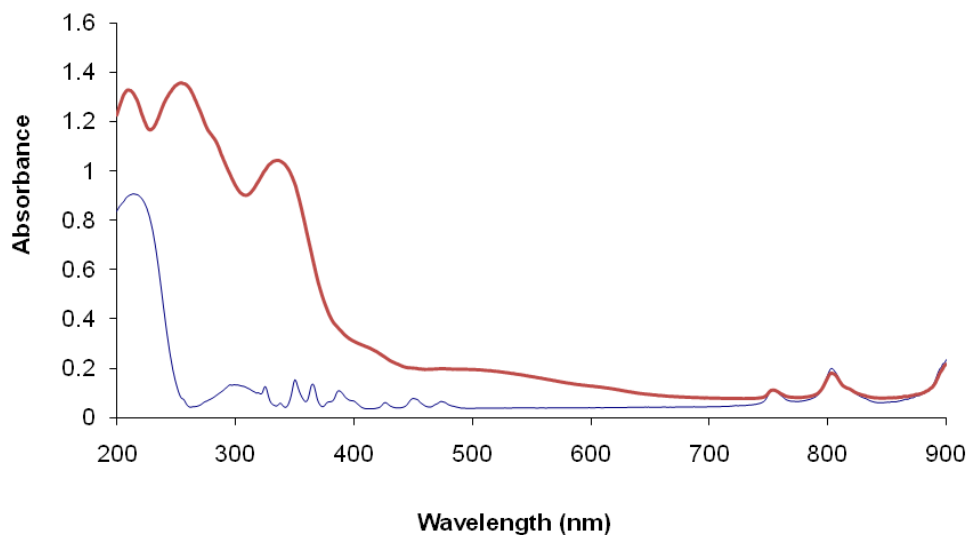


Figure 26 Ultra-violet absorption spectra of $\text{Dy}_2(\text{OH})_5\text{NO}_3 \cdot 1.5\text{H}_2\text{O}$ (shown in blue) and $\text{Dy}_2(\text{OH})_5(\text{AQDS})_{0.5} \cdot 3\text{H}_2\text{O}$ (shown in red).

Emission spectra for $\text{Dy}_2(\text{OH})_5\text{NO}_3 \cdot 1.5\text{H}_2\text{O}$ were measured by selective excitation at 220 and 300 nm, with greatest luminescent intensity achieved by excitation at 300 nm. The corresponding solid state emission spectrum is shown in Figure 27.

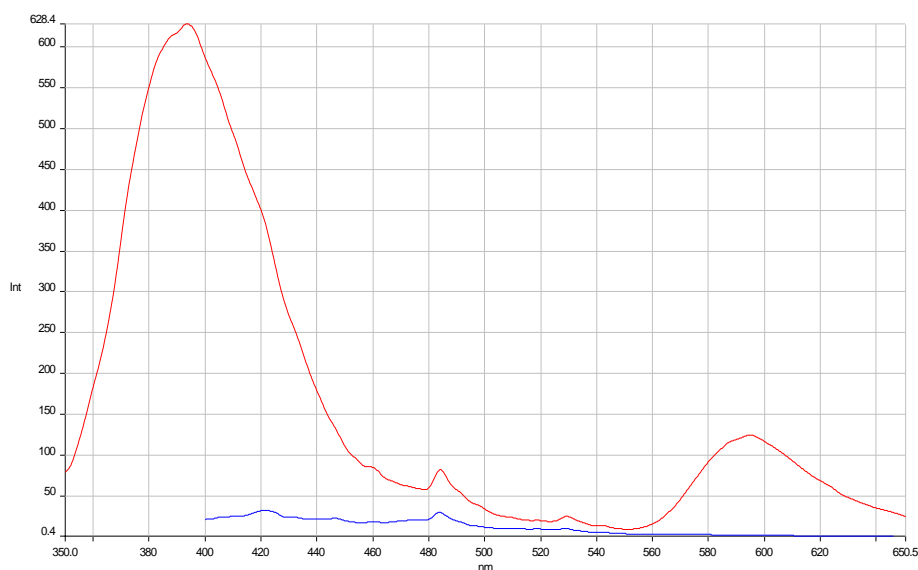


Figure 27 Emission spectra of $\text{Dy}_2(\text{OH})_5\text{NO}_3 \cdot 1.5\text{H}_2\text{O}$ (shown in red) and $\text{Dy}_2(\text{OH})_5(\text{AQDS})_{0.5} \cdot 3\text{H}_2\text{O}$ (shown in blue). $\lambda_{\text{ex}} = 300 \text{ nm}$.

The band observed at 395 nm and a weak emission band at 595 nm correspond to the characteristic emission from transitions of Dy^{3+} . The lifetime of these emissions however, were found to be too short to be measured. Once again the AQDS intercalate appears to completely quench emission, the reason for this is unclear but is possibly due to the fact that that 2,6-anthraquinonedisulfonate has an excited triplet state of lower energy than the Tb^{3+} emissive state. The quenching behaviour of some organics is known and has been used in sensor applications.^{36, 37}

As previously discussed, the synthesis of the potentially optically interesting $\text{Eu}_2(\text{OH})_5\text{NO}_3 \cdot 1.5\text{H}_2\text{O}$ was unsuccessful and so doping of Eu^{3+} cations into the crystalline $\text{Er}_2(\text{OH})_5\text{NO}_3 \cdot 1.5\text{H}_2\text{O}$ material was attempted. Eu was doped into the Er host material at levels of 70, 80 and 90 % using a hydrothermal method. Materials were characterised by XRD and elemental analysis. It was always found that Eu levels in the materials were lower than those intended, in the case of 70:30 Eu:Er levels of approximately 60:40 were in fact achieved.

Powder X-ray diffraction data and EDS results for the target composition $\text{Eu}_{1.4}\text{Er}_{0.6}(\text{OH})_5\text{NO}_3 \cdot 1.5\text{H}_2\text{O}$ are shown in Figure 28. The data confirm the presence of a single phase lamellar material with d-spacing 9.0 Å and a homogeneous dispersion of Eu^{3+} cations through the material at levels of ~ 59.5 %.

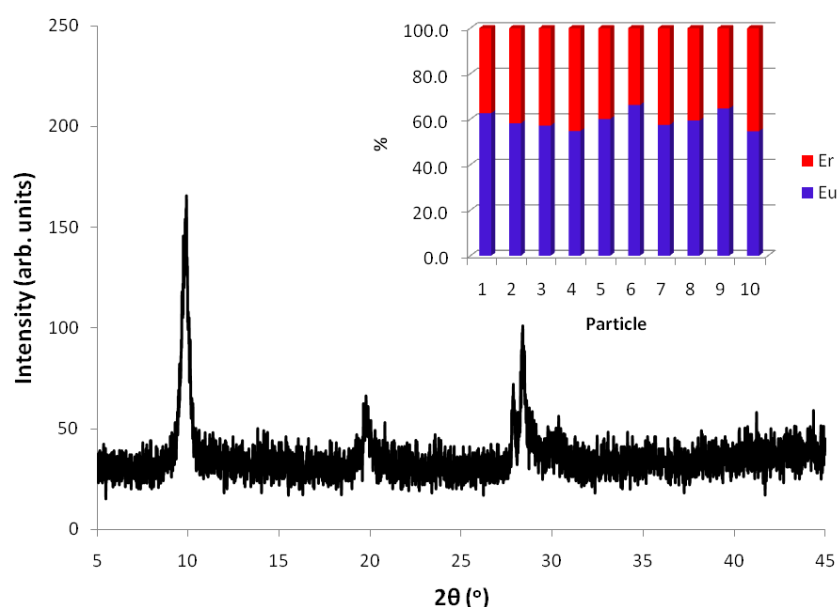


Figure 28 X-ray diffraction pattern for $\text{Eu}_{0.6}\text{Er}_{1.4}(\text{OH})_5\text{NO}_3 \cdot \text{H}_2\text{O}$. INSET EDS results showing homogeneous dispersion of Eu^{3+} cations within the $\text{Er}_2(\text{OH})_5\text{NO}_3 \cdot 1.5\text{H}_2\text{O}$ host lattice.

The ultra-violet absorption spectrum of $\text{Er}_{1.4}\text{Eu}_{0.6}(\text{OH})_5\text{NO}_3 \cdot 1.5\text{H}_2\text{O}$ is shown in Figure 29 and displays bands at 215 and 305 nm with a number of weaker absorptions in the region 350–800 nm.

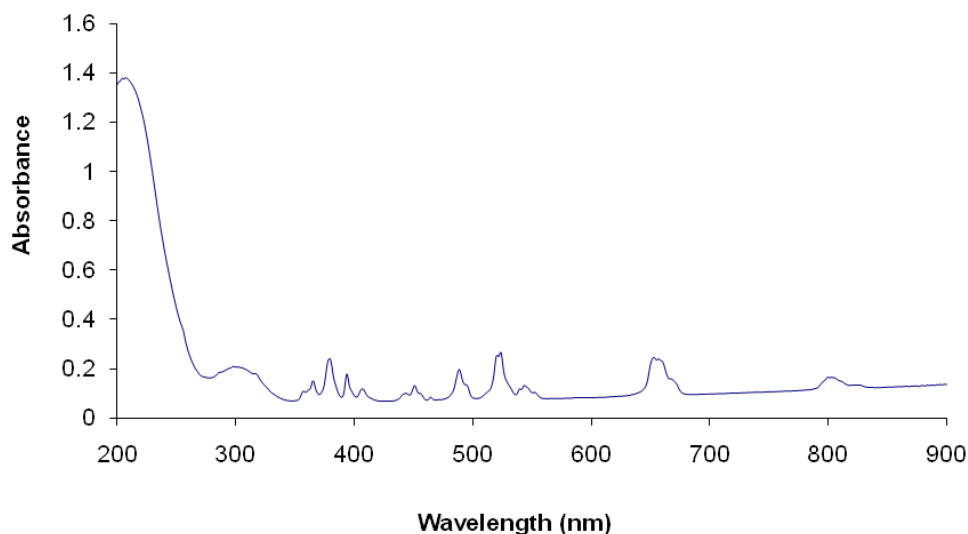


Figure 29 Ultra-violet absorption spectra of $\text{Eu}_{0.6}\text{Er}_{1.4}(\text{OH})_5\text{NO}_3 \cdot \text{H}_2\text{O}$.

Emission spectra for $\text{Er}_{1.4}\text{Eu}_{0.6}(\text{OH})_5\text{NO}_3 \cdot 1.5\text{H}_2\text{O}$ were measured by selective excitation at 290 and 350 nm, however emission was not observed at either of these wavelengths. It is thought that quenching by efficient non-radiative relaxation is responsible.

2.4 Hydroxyhalide Anion Exchange Materials, $\text{Ln}_2(\text{OH})_5\text{X} \cdot 1.5\text{H}_2\text{O}$ (X = Cl, Br; Ln = Y, Dy, Er, Yb)

2.4.1 Synthesis and Characterisation

Some of the work in the section was carried out by Erasmus student Leslie Poudret. Continuing the search for new hydroxy anion exchange materials it was decided to attempt the synthesis of halide containing host lattices. It was anticipated that these would possess less disorder within the interlayer gallery and thus aid structural

determination. The synthesis of $\text{Ln}_2(\text{OH})_5\text{X}\cdot 1.5\text{H}_2\text{O}$ ($\text{X} = \text{Cl}, \text{Br}$; $\text{Ln} = \text{Y}, \text{Dy}, \text{Er}, \text{Yb}$) was achieved via a hydrothermal route analogous to that used to prepare the hydroxynitrate materials. Typically an aqueous solution of $\text{LnX}_3\cdot n\text{H}_2\text{O}$ ($\text{X} = \text{Cl}, \text{Br}$; $\text{Ln} = \text{Y}, \text{La}, \text{Ce}, \text{Nd}, \text{Dy}, \text{Er}$ or Yb) was added to an aqueous solution containing NaOH and NaX ($\text{X} = \text{Cl}, \text{Br}$) and the resulting mixture treated hydrothermally at 150°C for 12 hours. As with the nitrate materials described earlier, it is thought that these materials possess a cation size limit. Again it was found that whilst the Y, Dy and Er phases were prepared pure, in spite of extensive reaction condition screening the Yb material was always biphasic. Reactions with the larger lanthanides yielded the previously reported $\text{Ln}_2(\text{OH})_2\text{Cl}$ phases.³⁸⁻⁴³

Powder XRD analysis of the $\text{Yb}_2(\text{OH})_5\text{Cl}\cdot 1.5\text{H}_2\text{O}$ sample, shown in Figure 30, revealed the presence of two phases in the sample with interlayer separations of 8.0 \AA and 8.4 \AA .

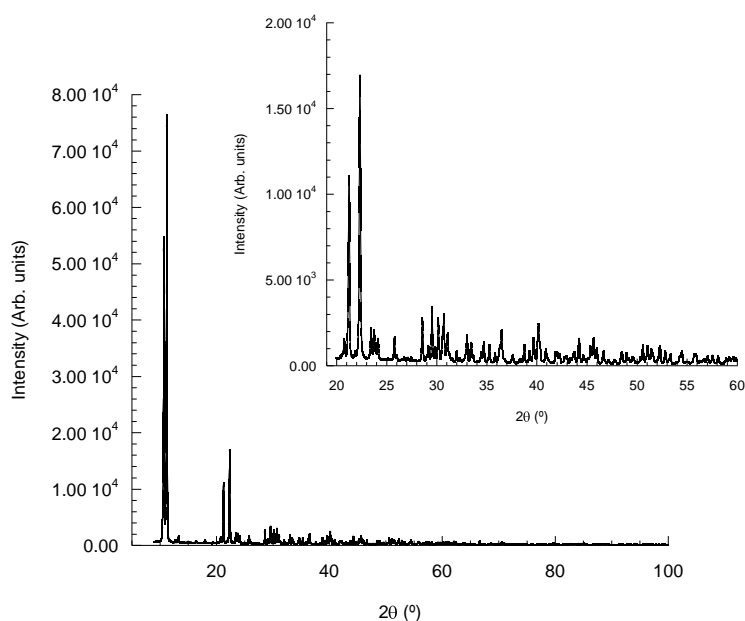
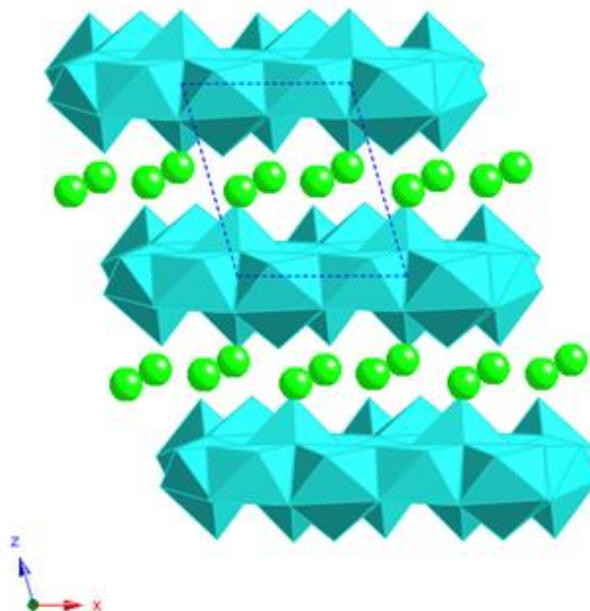


Figure 30 Powder X-ray diffraction pattern of $\text{Yb}_2(\text{OH})_5\text{Cl}\cdot 1.5\text{H}_2\text{O}$ showing two layered phases with interlayer separations of 8.03 \AA and 8.42 \AA .

The samples obtained were largely microcrystalline powders but very small single crystals of both phases were obtained. Structural refinements were carried out by Dr T. J. Prior following data collection at Station 9.8 of the U.K. SRS, Daresbury Laboratory. The structure of the 8.0 \AA phase is shown in Figure 31 and full

crystallographic details are given in Table 5, further crystallographic details are given in the Appendices.

a)



b)

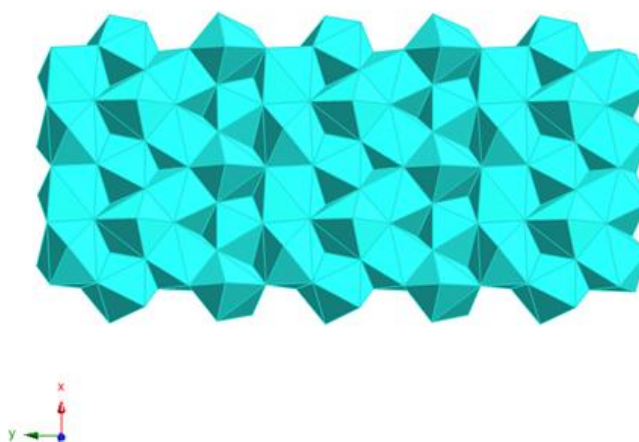


Figure 31 (a) Crystal structure and (b) layer structure of the 8.0 Å phase of $\text{Yb}_2(\text{OH})_5\text{Cl}\cdot 1.5\text{H}_2\text{O}$.

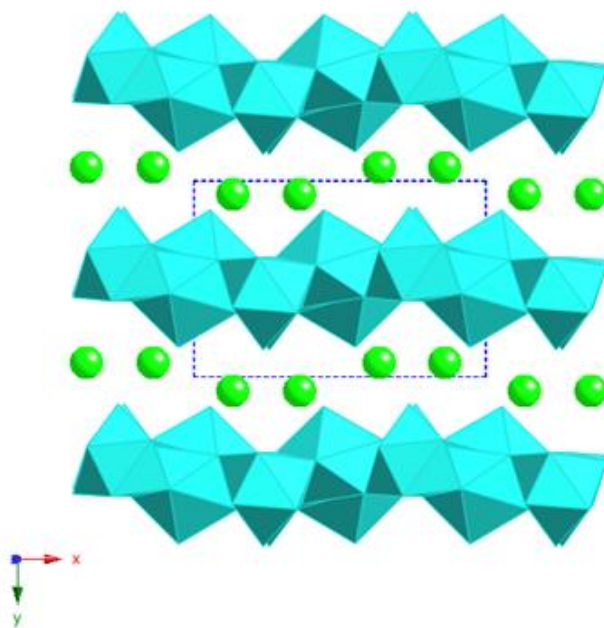
Table 5 Summary of the crystallographic information for the monoclinic and orthorhombic polymorphs of $\text{Yb}_2(\text{OH})_5\text{Cl}\cdot 1.5\text{H}_2\text{O}$.

Identification Code		8.4 Å phase	8 Å phase
Empirical formula		$\text{Cl}_2 \text{O}_{13} \text{Yb}_4$	$\text{Cl}_2 \text{O}_{13} \text{Yb}_4$
Formula weight		971.06	971.06
Temperature /K		120(2)	120(2)
Wavelength / Å		0.69430	0.69430
Crystal system		Orthorhombic	Monoclinic
Space group		$P c a 2_1$ (no. 29)	$P 2_1$ (no. 4)
Unit cell dimensions	a / Å	12.5108(10)	7.0245(7)
	b / Å	8.3930(13)	12.5199(12)
	c / Å	7.0438(10)	8.3174(8)
	$\alpha, \beta, \gamma / ^\circ$	90, 90, 90	90, 105.9750(10), 90
Volume / Å ³		739.62(17)	703.23(12)
Z		2	2
Density (calculated) / Mgm^{-3}		4.360	4.586
Absorption coefficient / mm^{-1}		25.467	26.784
F(000)		836	836
Crystal size / mm^3		$0.08 \times 0.01 \times 0.01$	$0.05 \times 0.04 \times 0.005$
Theta range for data collection / °		2.85 to 30.85	2.95 to 31.07
Index ranges		$-18 \leq h \leq 18, -12 \leq k \leq 12,$	$-10 \leq h \leq 10, -17 \leq k \leq 18,$
		$-10 \leq l \leq 10$	$-12 \leq l \leq 12$
Reflections collected		7946	8202
Independent reflections, R_{int}		1277, 0.0328	4201, 0.0390
Completeness to theta = 26.00°		98.7 %	99.5 %
Absorption correction		Semi-empirical from equivalents	Semi-empirical from equivalents
Max. and min. transmission		1.00 and 0.7242	0.875 and 0.276
Refinement method		Full-matrix least-squares on F^2	Full-matrix least-squares on F^2
Data / restraints / parameters		1277 / 43 / 91	4201 / 79 / 173
Goodness-of-fit on F^2		1.178	1.027
Final R indices [$I > 2\sigma(I)$]		$R_1 = 0.0330, wR_2 = 0.0685$	$R_1 = 0.0307, wR_2 = 0.0661$
R indices (all data)		$R_1 = 0.0410, wR_2 = 0.0733$	$R_1 = 0.0330, wR_2 = 0.0675$
Absolute structure parameter		-0.02(5)	0.33(2)
Largest diff. peak and hole / $e.\text{Å}^{-3}$		2.872 and -4.889	1.694 and -1.690

The 8.0 Å phase crystallises in the non-centrosymmetric monoclinic space group $P2_1$. The asymmetric unit contains four independent Yb ions and has the formula $\text{Yb}_4(\text{OH})_{10}(\text{H}_2\text{O})_3\text{Cl}_2$. The Yb and hydroxide ions assemble into dense positively charged layers of composition $[\text{Yb}_2(\text{OH})_5(\text{H}_2\text{O})_{1.5}]^+$ formed of eight and nine coordinate Yb with each hydroxide bridging between three Yb ions. Each Yb is bound to a large number of hydroxide ions: Yb1 and Yb4 each bind to eight hydroxide ions, while Yb2 and Yb3 bind to seven. Yb-OH distances lie in the range 2.222 to 2.522 Å. In addition to the hydroxide, water is also bound to Yb1, Yb2, and Yb3 and projects perpendicular to the layer at distances between 2.363 and 2.521 Å. The Yb cations can be considered to be arranged in rows along a . A bound water projects into the inter-layer region from three quarters of these rows; with a water absent from every fourth row. The layers are related by the 2_1 screw axis and stacked perpendicular to the ac plane at a separation $c\sin\beta$ (7.996(3) Å). This is slightly larger than those typically seen in the LDHs reflecting the thicker, buckled layers in this material.⁴⁴ Adjacent layers are displaced by 2.288(8) Å so they do not overlie (see Figure 31a). Located in the inter-layer region are charge-balancing chloride anions which form hydrogen bonds to hydroxide and water of the layers. For Cl1, three short hydrogen bonding contacts are identified and these lie in the range 3.10 to 3.26 Å (O...Cl distances). For Cl2, five short contacts are identified in the range 3.07 to 3.26 Å (O...Cl distances). In each case further, longer Cl...H-O contacts exist.

The layer structure reported here differs from that reported previously by Gandara *et al.*¹¹ due to the lower hydration level of the chloride intercalate giving rise to fewer nine coordinate polyhedra which alters the topology of the layer.

a)



b)

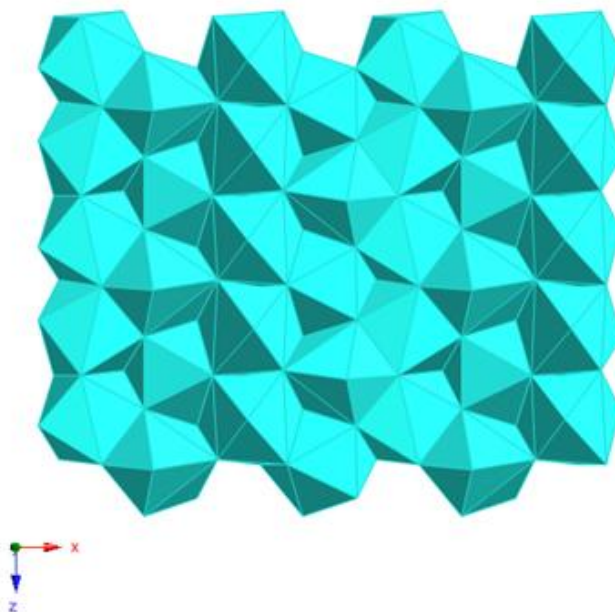


Figure 32 (a) Crystal structure and (b) layer structure of the 8.4 Å phase of $\text{Yb}_2(\text{OH})_5\text{Cl}\cdot 1.5\text{H}_2\text{O}$.

The “8.4 Å phase” crystallizes in the non-centrosymmetric orthorhombic space group $Pca2_1$ (no. 29) with an asymmetric unit of composition $Yb_2(OH)_5(H_2O)_{1.5}Cl$. Crystallographic details are given in the Appendices and the structure is illustrated in Figure 32. There are two independent Yb cations each coordinated by water and hydroxide, which bridges three Yb cations. Yb1 is coordinated by seven hydroxide ions and one fully occupied water molecule (O1w). Yb2 is coordinated by eight hydroxide ions and one half occupied water molecule (O2w). In a similar way to the 8 Å phase, the hydroxide and Yb cations form a dense layer with composition $[Yb_2(OH)_5(H_2O)_{1.5}]^+$, but the thickness of this layer varies slightly. Yb1 polyhedra share edges to form rows where the layer is two polyhedra thick, but Yb2 polyhedra share faces to form rows where the layer is one polyhedron thick.

When the structure is viewed down c (Figure 32a), an ordered arrangement of water in three quarters of rows similar to the 8 Å phase, can be seen. The middle row of each block of three contains only Yb2 and to these the half-occupancy water molecule is bound. One symmetry independent chloride ion is located between the layers and resides within a tight hydrogen bonding pocket shaped like a distorted octahedron formed from three hydroxide anions and three bound water molecules in a *fac* arrangement. One Cl...O distance is rather short (2.70 Å) signifying a strong hydrogen bond, while the others lie in the range 3.03 to 3.25 Å. Adjacent layers overlie and are related by a unit translation along b (interlayer distance 8.3930(13) Å) as shown in Figure 32a.

The layers in the 8.0 Å and 8.4 Å phases are similar but differ because of slight changes in the orientation of the polyhedra within the layer and hence their thickness. The basic motif is very similar but the presence of disordered water (O2w) in the 8.4 Å phase leads to local differences. In neither crystal structure is there evidence for unbound water located between the layers. The use of PLATON suggests that there are no solvent accessible voids in either structure.⁴⁵

The composition of these materials was confirmed by elemental analysis and TGA, characterising data is summarized in Table 6.

Table 6 Characterising data for the new lanthanide hydroxyhalides, $\text{Ln}_2(\text{OH})_5\text{X}\cdot 1.5\text{H}_2\text{O}$.

Ln, X	Composition	Interlayer Separation (Å)	Elemental Analysis	
			Observed (%)	Calculated (%)
Y, Cl	$\text{Y}_2(\text{OH})_5\text{Cl}\cdot 1.5\text{H}_2\text{O}$	8.37	Y (53.74)	Y (54.66)
			H (2.40)	H (2.48)
Dy, Cl	$\text{Dy}_2(\text{OH})_5\text{Cl}\cdot 1.5\text{H}_2\text{O}$	8.41	Dy (68.46)	Dy (68.78)
			H (1.61)	H (1.71)
Er, Cl	$\text{Er}_2(\text{OH})_5\text{Cl}\cdot 1.5\text{H}_2\text{O}$	8.39	Er (69.40)	Er (73.63)
			H (1.55)	H (1.67)
Yb, Cl	$\text{Yb}_2(\text{OH})_5\text{Cl}\cdot 1.5\text{H}_2\text{O}$	8.42, 8.00	Yb (69.88)	Yb (70.11)
			H (1.53)	H (1.63)
Y, Br	$\text{Y}_2(\text{OH})_5\text{Br}\cdot 1.5\text{H}_2\text{O}$	8.35	Y (47.26)	Y (48.09)
			H (2.11)	H (2.18)
Yb, Br	$\text{Yb}_2(\text{OH})_5\text{Br}\cdot 1.5\text{H}_2\text{O}$	8.33, 8.77	Yb (64.20)	Yb (64.32)
			H (1.42)	H (1.50)

The TGA trace for $\text{Er}_2(\text{OH})_5\text{Cl}\cdot 1.5\text{H}_2\text{O}$ is shown in Figure 33 and displays two mass losses. The first mass loss of 5.5 % (calculated value for $x = 1.5$ is 5.6 %) below 200 °C corresponds to the loss of co-intercalated water. A further mass loss of 9.0 % (9.3 %) by 600 °C is observed resulting from the decomposition of the hydroxide layers. No significant further mass losses are observed above this temperature and PXRD of the final material reveals a mixture of Er_2O_3 and ErOCl .

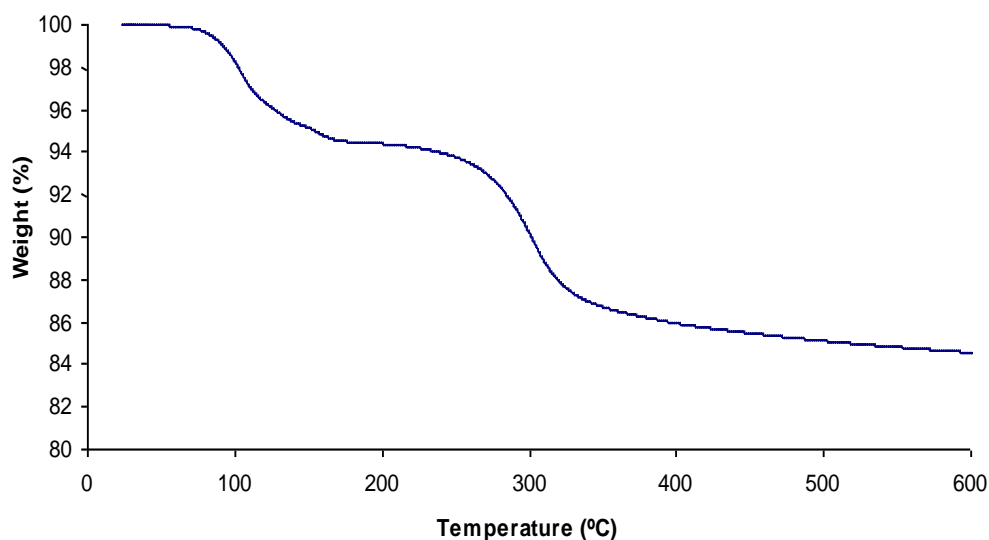


Figure 33 TGA trace for $\text{Er}_2(\text{OH})_5\text{Cl}\cdot 1.5\text{H}_2\text{O}$ showing mass losses of 5.5 % below 200 °C and a further mass loss of 9.0 % by 600 °C.

Notably, the same synthetic conditions that give biphasic materials with Yb, when utilized for the Y, Dy and Er materials yielded only the 8.4 Å phase, with no evidence for the formation of the 8.0 Å in the XRD pattern, Figure 34a.

The analogous $\text{Ln}_2(\text{OH})_5\text{Br}\cdot 1.5\text{H}_2\text{O}$ materials were obtained by hydrothermal synthesis where $\text{LnCl}_3\cdot n\text{H}_2\text{O}$ was replaced by $\text{LnBr}_3\cdot n\text{H}_2\text{O}$ ($\text{Ln} = \text{Y}, \text{Yb}$). Similarly to the hydroxychlorides the Yb material was found to be biphasic with correspondingly larger interlayer separations due to the increased size of the bromide anion, $d = 8.33$ Å and 8.77 Å, whereas the Y material was phase pure. Further to this expected change in layer spacing, the interlayer anion in the case of the Y material also dictates the structural symmetry. $\text{Y}_2(\text{OH})_5\text{Br}\cdot 1.5\text{H}_2\text{O}$ exists as the monoclinic 8.0 Å phase whereas $\text{Y}_2(\text{OH})_5\text{Cl}\cdot 1.5\text{H}_2\text{O}$ is found as the orthorhombic 8.4 Å phase, suggesting that there is a subtle interplay between cation size and therefore the layer thickness and the hydrogen bonding between the guest anion and the layers.

2.4.2 Anion Exchange Reactions

Anion exchange reactions for these hydroxyhalides with a range of dicarboxylate salts were successful at room temperature. Powder X-ray diffraction and chemical analysis data demonstrate that $\text{Er}_2(\text{OH})_5\text{Cl}\cdot 1.5\text{H}_2\text{O}$ undergoes complete exchange at room temperature. Diffraction peaks characteristic of the host material were completely replaced by others of larger d-spacing, indicating guest intercalation. Reactions proceeded with the maleate, phthalate, terephthalate and succinate anions forming materials with the composition $\text{Er}_2(\text{OH})_5(\text{guest})_{0.5}\cdot 1.5\text{H}_2\text{O}$. The powder X-ray diffraction pattern for the anion exchange products of $\text{Er}_2(\text{OH})_5(o\text{-C}_8\text{H}_4\text{O}_4)_{0.5}\cdot 1.5\text{H}_2\text{O}$ are shown in Figure 34b and the characterising data for additional anion exchange reactions is given in Table 7.

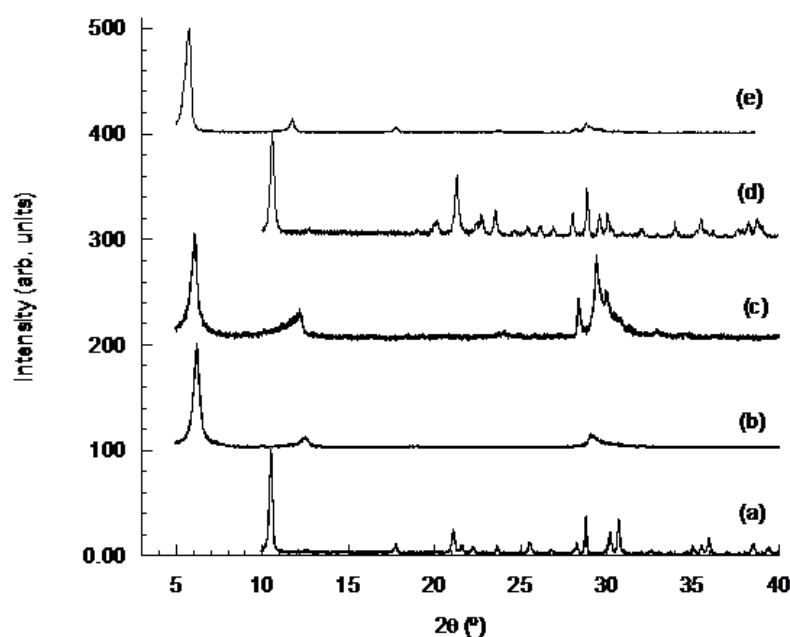


Figure 34 Powder X-ray diffraction patterns of:

- (a) $\text{Er}_2(\text{OH})_5\text{Cl}\cdot 1.5\text{H}_2\text{O}$ and the anion exchange intercalation compounds
- (b) $\text{Er}_2(\text{OH})_5(o\text{-C}_8\text{H}_4\text{O}_4)_{0.5}\cdot 1.5\text{H}_2\text{O}$,
- (c) $\text{Yb}_2(\text{OH})_5(o\text{-C}_8\text{H}_4\text{O}_4)_{0.5}\cdot 1.5\text{H}_2\text{O}$ showing a single phase following anion exchange,
- (d) $\text{Y}_2(\text{OH})_5\text{Br}\cdot 1.5\text{H}_2\text{O}$ and
- (e) the anion exchange derivative $\text{Y}_2(\text{OH})_5(o\text{-C}_8\text{H}_4\text{O}_4)_{0.5}\cdot 1.5\text{H}_2\text{O}$.

The interlayer separations observed for these compounds are comparable to those seen for other dicarboxylate intercalates of layered hydroxides.¹⁸ Both phases of the biphasic $\text{Yb}_2(\text{OH})_5\text{Cl}\cdot 1.5\text{H}_2\text{O}$ material demonstrated anion exchange with succinate, maleate, phthalate and terephthalate forming a single product, as can be seen in Figure 34c. The observation of single phase product from these anion exchange reactions reflects the polymorphic relationship between the two $\text{Yb}_2(\text{OH})_5\text{Cl}\cdot 1.5\text{H}_2\text{O}$ phases. The ease of anion exchange in these materials is comparable to that seen in the $\text{Ln}_2(\text{OH})_5\text{NO}_3\cdot 1.5\text{H}_2\text{O}$ phases and occurs more readily than for $\text{La}(\text{OH})_2\text{NO}_3$ which required prolonged heating at 65 °C to bring about complete exchange.⁷ These observations are consistent with the different coordination environments of the intercalated anions in these systems with the more forcing conditions required when the anion is directly coordinated to the metal cation in the layer.

Table 7 Characterising data for the anion exchange derivatives of $\text{Er}_2(\text{OH})_5\text{Cl}\cdot 1.5\text{H}_2\text{O}$.

Guest	Composition	Interlayer Separation (Å)	Elemental Analysis	
			Observed (%)	Calculated (%)
Succinate	$\text{Er}_2(\text{OH})_5(\text{C}_4\text{H}_4\text{O}_4)_{0.5}\cdot 1.5\text{H}_2\text{O}$	11.72	Er (66.08)	Er (66.29)
			C (4.75)	C (4.76)
			H (1.96)	H (2.00)
Maleate	$\text{Er}_2(\text{OH})_5(\text{cis-}\text{C}_4\text{H}_2\text{O}_4)_{0.5}\cdot 1.5\text{H}_2\text{O}$	10.22	Er (66.13)	Er (66.42)
			C (4.87)	C (4.77)
			H (1.74)	H (1.80)
Phthalate	$\text{Er}_2(\text{OH})_5(\text{o-}\text{C}_8\text{H}_4\text{O}_4)_{0.5}\cdot 1.5\text{H}_2\text{O}$	14.09	Er (62.89)	Er (63.28)
			C (9.22)	C (9.09)
			H (1.97)	H (1.91)
Terephthalate	$\text{Er}_2(\text{OH})_5(\text{p-}\text{C}_8\text{H}_4\text{O}_4)_{0.5}\cdot 1.5\text{H}_2\text{O}$	12.95	Er (63.00)	Er (63.28)
			C (8.81)	C (9.09)
			H (1.81)	H (1.91)

Further characterisation of the anion exchange derivatives was achieved by FTIR spectroscopy as shown in Figure 35 for $Y_2(OH)_5(o-C_8H_4O_4)_{0.5} \cdot 1.5H_2O$. Strong absorptions at approximately 1550 cm^{-1} and 1400 cm^{-1} correspond to the symmetric and asymmetric stretches, respectively, of the carboxylate groups of the intercalated phthalate anion. The positions of these bands are consistent with observations made on other layered hydroxide systems intercalated with carboxylate anions.⁴⁶

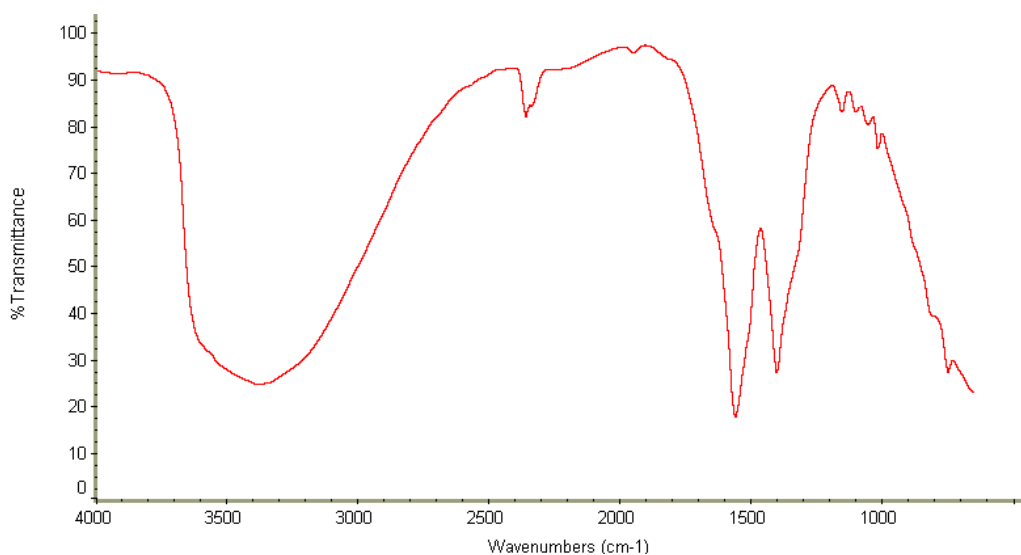


Figure 35 FTIR spectrum of $Y_2(OH)_5(o-C_8H_4O_4)_{0.5} \cdot 1.5H_2O$.

The hydroxybromide materials also undergo intercalation reactions, with room temperature anion exchange observed with maleate, phthalate, terephthalate and succinate anions. A comparison of the anion exchange products from the chloride and bromide hosts can be made from the powder X-ray diffraction patterns shown in Figure 34d and Figure 34e, from which it can be seen that the same material is formed in each case suggesting that the layer structure is the same in both the lanthanide hydroxychlorides and hydroxybromides.

2.5 Conclusions

$\text{Ln}_2(\text{OH})_5\text{NO}_3 \cdot 1.5\text{H}_2\text{O}$ ($\text{Ln} = \text{Y}, \text{Gd} - \text{Lu}; x \approx 1 - 1.5$) - a new family of anion exchange intercalation hosts have been synthesised via a hydrothermal route and fully characterised. These are first lamellar host lattices to incorporate the smaller lanthanide cations within the layers. These intercalation hosts have been shown to undergo facile exchange reactions with a wide range of organic carboxylate and sulfonate anions.

They have been found to preferentially intercalate *cis*- $\text{C}_4\text{H}_2\text{O}_4$ from equimolar mixture of *cis*- and *trans*- isomers at levels of 84-89 % and for *ortho*- and *para*- $\text{C}_8\text{H}_4\text{O}_4$ mixtures, *ortho*- $\text{C}_8\text{H}_4\text{O}_4$ is favoured at levels of 56-77 %. Whilst the structure of $\text{Ln}_2(\text{OH})_5\text{NO}_3 \cdot 1.5\text{H}_2\text{O}$ materials are unknown, analysis of the analogous YNDS $[\text{Y}_4(\text{OH})_{10}(\text{H}_2\text{O})_4]^{2+}$ layer revealed the likely contributing factors. It is suggested that the selectivity preferences displayed are likely to result from the presence of water molecules which protrude from the lanthanide hydroxide layer causing an irregular hydrogen bonding surface, giving rise to anion binding in a non-perpendicular fashion to the 2D layer. The carboxylate anions of maleate and phthalate are expected to be significantly tilted with respect to the layer, thus enabling these anions to project both carboxylates towards the same layer face, allowing both to be involved in hydrogen bonding and hence maximising electrostatic interactions. High levels of selectivity comparable with those previously observed in LDHs are not observed owing to the fact that fumarate and terephthalate are still able to bridge across hydroxide layers. Consequently, the binding of both isomers is energetically similar overall. A possible explanation for the higher levels of *cis*-selectivity observed is the difference in hydrogen-bonding interaction “heights” between maleate and phthalate anions and the greater flexibility of the maleate anion compared with phthalate.

Luminescence experiments on Tb and Dy materials demonstrated that $\text{Tb}_2(\text{OH})_5\text{NO}_3 \cdot 1.5\text{H}_2\text{O}$ is the most optically active but has a very short emission lifetime of just 0.038 ms. These disappointing results are thought to be due to the

$\nu(\text{O-H})$ vibration of the coordinated H_2O molecules and hydroxide anions which lead to non-radiative relaxation of the excited state.

Finally the $[\text{Ln}_2(\text{OH})_5]^+$ family of layered materials have been expanded to include $\text{Ln}_2(\text{OH})_5\text{X}\cdot 1.5\text{H}_2\text{O}$ ($\text{X} = \text{Cl}, \text{Br}$; $\text{Ln} = \text{Y}, \text{Dy}, \text{Er}, \text{Yb}$) synthesised via a hydrothermal route. $\text{Yb}_2(\text{OH})_5\text{Cl}\cdot 1.5\text{H}_2\text{O}$ is biphasic with d-spacings of 8.0 Å and 8.4 Å. Single crystal diffraction studies showed that one Yb polymorph is monoclinic and the other orthorhombic. The orthorhombic structure is adopted by the other lanthanide hydroxychloride hosts. In both cases the layer composition is the same and both contain 8- and 9-coordinate Yb sites with bridging hydroxide groups and coordinated water molecules. The structures differ in the arrangement of layers and presence of water projecting from the layer which leads to different hydrogen bonding to guest anions. These structures are the first determined for the $m = 1$ members of the $\text{Ln}_2(\text{OH})_{6-m}(\text{A})_m\cdot n\text{H}_2\text{O}$ family of intercalation hosts. $\text{Yb}_2(\text{OH})_5\text{Br}\cdot 1.5\text{H}_2\text{O}$ is also biphasic displaying larger interlayer separations of 8.33 Å and 8.77 Å although in this case $\text{Y}_2(\text{OH})_5\text{Br}\cdot 1.5\text{H}_2\text{O}$ forms the phase with the smaller interlayer spacing. These materials are also found to undergo facile anion exchange reactions with a range of organic dicarboxylate anions.

2.6 Recent Developments

The synthesis, characterisation and anion exchange reactions of the new family of $\text{Ln}_2(\text{OH})_5\text{NO}_3\cdot 1.5\text{H}_2\text{O}$ ($\text{Ln} = \text{Y}, \text{Gd} - \text{Lu}$) materials was published in 2008 (see Appendix C). At this time these lamellar host lattices were the first to incorporate the smaller lanthanide cations within the layers with fully exchangeable interlayer anions. Since this time a number of groups have made advances in the field and for completeness these are reviewed here.

Geng *et al.* reported a layered hydroxychloride incorporating europium cations with the composition $\text{Eu}(\text{OH})_{2.5}\text{Cl}\cdot 0.8\text{H}_2\text{O}$.⁴⁷ The material was synthesised via the homogeneous precipitation of $\text{EuCl}_3\cdot x\text{H}_2\text{O}$ and hexamethylenetetramine (HMT). Structural determination by Rietveld analysis revealed an orthorhombic unit cell with parameters of $a = 12.92(1)$ Å, $b = 7.38(1)$ Å and $c = 8.71(1)$ Å in which the formula

unit is $\text{Eu}_8(\text{OH})_{20}\text{Cl}_4 \cdot 6.4\text{H}_2\text{O}$. $[\text{Eu}_8(\text{OH})_{20}]^{4+}$ cationic layers consist of three Eu coordination environments, two of which are 9-coordinated to 8 hydroxy groups and one water molecule with the other 8-coordinated to 7 hydroxy groups and one water molecule. The interlayer chloride anions readily undergo anion exchange with NO_3^- , SO_4^{2-} and $\text{C}_{12}\text{H}_{25}\text{OSO}_3^-$ under ambient conditions. Results of optical experiments were reported for the first Eu containing layered hydroxide, in which the authors observe a series of sharp lines in the emission spectra typical of Eu^{3+} 4f-4f transitions. Luminescence from the higher excited levels however was not detected and this is thought to be as a consequence of a very efficient non-radiative relaxation to the $^5\text{D}_0$ level. More recently the synthesis has been expanded and includes some of the larger lanthanides with the composition $\text{Ln}_8(\text{OH})_{20}\text{Cl}_4 \cdot n\text{H}_2\text{O}$ ($\text{Ln} = \text{Nd}, \text{Sm}, \text{Gd} - \text{Tm}$ and Y).⁴⁸ A cation size limit is also indicated for this phase given that the materials containing the larger Nd and the smaller Tm could not be synthesised phase pure. The authors also suggest that the formation of the phases is highly dependent on humidity levels during the drying process. Preliminary Tb luminescence experiments suggest that the material may have potential for use in optical devices, however lifetimes of emission are not given nor are the anion exchange properties investigated.

The sensitivity of the hydrothermal synthesis method is well known and is highlighted by the ability of Lee *et al.* to extend the $\text{Ln}_2(\text{OH})_5\text{NO}_3 \cdot x\text{H}_2\text{O}$ family to include $\text{Ln} = \text{Gd}, \text{Eu}$ and Sm ($x = 1 - 1.5$ depending on drying conditions). The materials of identical composition are formed hydrothermally where pH is in the optimal range 6.7 – 7.2.⁴⁹ Reactions at higher pH yield large amounts of $\text{Ln}(\text{OH})_3$ and those at lower pH values give low product yields. Analogous syntheses for La and Nd materials proved unsuccessful. Anion exchange reactions with a wide range of organic sulfates, sulfonates and carbonates were facile, but those with short alkyl chains required heating as these reactions proceeded slowly. Investigations into the magnetic properties of the $\text{Gd}_2(\text{OH})_5\text{NO}_3 \cdot \text{H}_2\text{O}$ and $\text{Gd}_2(\text{OH})_5(\text{C}_{10}\text{H}_{21}\text{SO}_3) \cdot 1.5\text{H}_2\text{O}$ revealed paramagnetic behaviour.

The paramagnetic behaviour of Gd^{3+} cations has been further investigated by Lee *et al.* where aqueous suspensions of layered gadolinium hydroxychloride $\text{Gd}_2(\text{OH})_5\text{Cl} \cdot 1.5\text{H}_2\text{O}$, synthesised by refluxing $\text{GdCl}_3 \cdot 6\text{H}_2\text{O}$ with KOH, have been reported as a potential MRI contrast agents.⁵⁰ The material is cited as a suitable T_1

contrast agents for MRI cell tracking but further work is needed to improve its stability at low pH.

$Y_2(OH)_5NO_3 \cdot 1.5H_2O$ prepared by a sonochemical method has been utilized as an efficient sorbent in the removal of Cr(VI) from water.⁵¹ The lanthanide hydroxynitrate materials described in this chapter are also included in recent reviews concerning lanthanide-containing light-emitting organic-inorganic hybrids and cationic inorganic materials with potential applications in anionic pollutant trapping and catalysis.⁵²⁻⁵⁴

2.7 References

1. Z. Chang, D. Evans, X. Duan, P. Boutinaud, M. de Roy and C. Forano, *Journal of Physics and Chemistry of Solids*, 2006, **67**, 1054-1057.
2. S. Gago, M. Pillinger, R. A. S. Ferreira, L. D. Carlos, T. M. Santos and I. S. Goncalves, *Chemistry of Materials*, 2005, **17**, 5803-5809.
3. D. Louer and M. Louer, *Journal of Solid State Chemistry*, 1987, **68**, 292-299.
4. M. Louer, D. Louer, A. L. Delgado and O. G. Martinez, *European Journal of Solid State and Inorganic Chemistry*, 1989, **26**, 241-253.
5. M. Lundberg and A. J. Skarnulis, *Acta Crystallographica Section B-Structural Science*, 1976, **32**, 2944-2947.
6. D. F. Mullica, E. L. Sappenfield and D. A. Grossie, *Journal of Solid State Chemistry*, 1986, **63**, 231-236.
7. S. P. Newman and W. Jones, *Journal of Solid State Chemistry*, 1999, **148**, 26-40.
8. J. M. Haschke, *Inorganic Chemistry*, 1974, **13**, 1812-1818.
9. C. E. Holcombe, *Journal of the American Ceramic Society*, 1978, **61**, 481-486.
10. I. Schildermans, J. Mullens, J. Yperman, D. Franco and L. C. Vanpoucke, *Thermochimica Acta*, 1994, **231**, 185-192.
11. F. Gandara, J. Perles, N. Snejko, M. Iglesias, B. Gomez-Lor, E. Gutierrez-Puebla and M. A. Monge, *Angewandte Chemie-International Edition*, 2006, **45**, 7998-8001.
12. J. G. Bunzli, E. Moret and J. Yersin, *Helvetica Chimica Acta*, 1978, **61**, 762.

13. A. M. Fogg, J. Meldrum, G. R. Darling, J. B. Claridge and M. J. Rosseinsky, *Journal of the American Chemical Society*, 2006, **128**, 10043-10053.
14. A. M. Fogg, G. R. Williams, R. Chester and D. O'Hare, *Journal of Materials Chemistry*, 2004, **14**, 2369-2371.
15. M. S. C. Flett, *Journal of the Chemical Society*, 1951, 962-967.
16. F. Kooli, I. C. Chisem, M. Vucelic and W. Jones, *Chemistry of Materials*, 1996, **8**, 1969-1977.
17. M. Borja and P. K. Dutta, *Journal of Physical Chemistry*, 1992, **96**, 5434-5444.
18. G. R. Williams, T. G. Dunbar, A. J. Beer, A. M. Fogg and D. O'Hare, *Journal of Materials Chemistry*, 2006, **16**, 1222-1230.
19. A. M. Fogg, J. S. Dunn, S. G. Shyu, D. R. Cary and D. O'Hare, *Chemistry of Materials*, 1998, **10**, 351-355.
20. A. M. Fogg, V. M. Green, H. G. Harvey and D. O'Hare, *Advanced Materials*, 1999, **11**, 1466-1469.
21. L. X. Lei, A. Khan and D. O'Hare, *Journal of Solid State Chemistry*, 2005, **178**, 3648-3654.
22. A. Ragavan, A. Khan and D. O'Hare, *Journal of Materials Chemistry*, 2006, **16**, 4155-4159.
23. A. Ragavan, A. I. Khan and D. O'Hare, *Journal of Materials Chemistry*, 2006, **16**, 602-608.
24. G. R. Williams, T. G. Dunbar, A. J. Beer, A. M. Fogg and D. O'Hare, *Journal of Materials Chemistry*, 2006, **16**, 1231-1237.
25. F. Millange, R. I. Walton, L. X. Lei and D. O'Hare, *Chemistry of Materials*, 2000, **12**, 1990-1994.
26. A. Ragavan, A. Khan and D. O'Hare, *Journal of Materials Chemistry*, 2006, **16**.
27. O. Buyukgungor and M. Odabasoglu, *Acta Crystallographica Section C: Crystal Structure Communications*, 2003, **59**, 105.
28. Z. M. Jin, Y. J. Pan, M. L. Hu and S. Liang, *Journal of Chemical Crystallography*, 2001, **31**, 191.
29. B. Yan, Y. S. Song and Z. X. Chen, *Journal of Molecular Structure*, 2004, **694**, 115-120.
30. G. Stein and E. Wurzburg, *Journal of Chemical Physics*, 1975, **62**, 208-213.

31. Y. Matsumoto, U. Unal, Y. Kimura, S. Ohashi and K. Izawa, *Journal of Physical Chemistry B*, 2005, **109**, 12748-12754.
32. T. C. Ozawa, K. Fukuda, K. Akatsuka, Y. Ebina and T. Sasaki, *Chemistry of Materials*, 2007, **19**, 6575-6580.
33. H. C. Aspinall, *Chemistry of the f-Block Elements*, Gordon and Breach Science Publishers, Singapore, 2001.
34. F. Serpaggi, T. Luxbacher, A. K. Cheetham and G. Ferey, *Journal of Solid State Chemistry*, 1999, **145**, 580-586.
35. M. D. Allendorf, C. A. Bauer, R. K. Bhakta and R. T. J. Houk, *Chemical Society Reviews*, 2009, **38**, 1330-1352.
36. T. Ogoshi and A. Harada, *Sensors*, 2008, **8**, 4961-4982.
37. W. S. Xia, R. H. Schmehl and C. J. Li, *Tetrahedron*, 2000, **56**, 7045-7049.
38. V. I. Bukin, *Doklady Akademii Nauk Sssr*, 1972, **207**, 1332-1335.
39. F. L. Carter and S. Levinson, *Inorganic Chemistry*, 1969, **8**, 2788-&.
40. K. Dornberger-Schiff and R. F. Klevtsova, *Acta Crystallographica*, 1967, **22**, 435.
41. C. Jouve, J. Marrot and D. Riou, *Acta Crystallographica Section C-Crystal Structure Communications*, 2002, **58**, I14-I15.
42. R. F. Klevtsova and L. A. Z. Glinskaya, *Zhurnal Strukturnoi Khimii*, 1969, **10**, 494.
43. T. N. Tarkhova, I. A. Grishin and N. N. Mironov, *Zhurnal Neorganicheskoi Khimii*, 1970, **15**, 2584-&.
44. A. V. Besserguenev, A. M. Fogg, R. J. Francis, S. J. Price, D. O'Hare, V. P. Isupov and B. P. Tolochko, *Chemistry of Materials*, 1997, **9**, 241.
45. A. L. Speck, *Journal of Applied Crystallography*, 2003, **36**, 7-13.
46. F. Li, F. H. Zhang, D. G. Evans, C. Forano and X. Duan, *Thermochimica Acta*, 2004, **424**, 15-23.
47. F. X. Geng, H. Xin, Y. Matsushita, R. Z. Ma, M. Tanaka, F. Izumi, N. Iyi and T. Sasaki, *Chemistry-a European Journal*, 2008, **14**, 9255-9260.
48. F. X. Geng, Y. Matsushita, R. Z. Mat, H. Xin, M. Tanaka, F. Izumi, N. Iyi and T. Sasaki, *Journal of the American Chemical Society*, 2008, **130**, 16344-16350.
49. K. H. Lee and S. H. Byeon, *European Journal of Inorganic Chemistry*, 2009, 929-936.

50. B. I. Lee, K. S. Lee, J. H. Lee, I. S. Lee and S. H. Byeon, *Dalton Transactions*, 2009, 2490-2495.
51. H. M. Zhong, Y. L. Ma, X. F. Cao, X. T. Chen and Z. L. Xue, *Journal of Physical Chemistry C*, 2009, **113**, 3461-3466.
52. E. Brunet, H. M. H. Alhendawi, O. Juanes, L. Jimenez and J. C. Rodriguez-Ubis, *Journal of Materials Chemistry*, 2009, **19**, 2494-2502.
53. L. D. Carlos, R. A. S. Ferreira, V. D. Bermudez and S. J. L. Ribeiro, *Advanced Materials*, 2009, **21**, 509-534.
54. S. R. J. Oliver, *Chemical Society Reviews*, 2009, **38**, 1868-1881.